Available online at www.sciencedirect.com

ScienceDirect

ELSEVIER

European Journal of Mechanics B/Fluids 26 (2007) 583–614

EUROPEAN JOURNAL OF MECHANICS B/FLUIDS

Experimental study of the near field and transition region of a free jet issuing from a sharp-edged elliptic orifice plate

W.R. Quinn

Department of Engineering, St. Francis Xavier University, Antigonish, Nova Scotia, Canada B2G 2W5

Received 9 December 2005; received in revised form 6 October 2006; accepted 26 October 2006

Abstract

The mixing characteristics in the near field and transition region, the region of interest in most jet mixing applications, of an isothermal, incompressible, free jet of air issuing from a sharp-edged elliptic orifice plate of aspect ratio 2 into still air surroundings have been studied experimentally using hot-wire anemometry and a pitot-static tube. For comparison, some experiments were performed in round jets issuing from a sharp-edged orifice plate and from a contoured nozzle. All the test jets were unforced and the Reynolds number, based on the equivalent diameter of the sharp-edged elliptic orifice plate which was the same as the diameter of the sharp-edged round orifice plate or the contoured round nozzle, was 1.88×10^5. The three components of the mean velocity vector, time-averaged and phase-averaged fluctuating velocity data, autocorrelation coefficients and one-dimensional spectra of the fluctuating velocities and the mean static pressure were measured. The mean streamwise vorticity, mass entrainment rates and the jet half-velocity widths have been obtained from the measured data. The results show that mixing in an elliptic jet issuing from a sharp-edged orifice plate is higher than in round jets and in elliptic jets issuing from contoured nozzles. The near field and transition region of the elliptic jet were deduced to be dominated by the axisymmetric instability mode which triggers the generation of symmetric shear layer structures. The results also show the presence of coherent structures in the near field and transition region of the jet and the effect of these coherent structures on momentum transport in the jet.

Keywords: Jets; Elliptic; Sharp-edged orifice plate; Mixing; Turbulence

1. Introduction

Turbulent free jets can be found in several applications in aerospace, chemical and mechanical engineering. In aerospace engineering, for example, these jets are used for thrust vectoring and upper surface blowing. It may, for ease of manufacturing and installation, be necessary for the jets in some applications to issue from orifii, cut in flat surfaces, with sharp edges. There is also some evidence (Quinn and Militzer [1], Mi et al. [2], Quinn [3]) that jets issuing from sharp-edged orifice plates entrain more ambient fluid and, therefore, have better mixing characteristics than those emanating from contoured nozzles. A sharp-edged orifice plate is, therefore, used in the present study. Mixing in the context of the present study, in which both the jet fluid and the ambient fluid are the same and are both

---

E-mail address: wquinn@stfx.ca (W.R. Quinn).

doi:10.1016/j.euromechflu.2006.10.005

unheated, should be understood as the entrainment of ambient fluid by the jet fluid and momentum transfer within the jet fluid as the jet evolves.

Non-circular jets have been found (Gutmark and Grinstein [4]) to entrain significantly more ambient fluid than their round counterparts. These jets have, therefore, emerged as effective passive flow control devices. Jets issuing from contoured elliptic nozzles have thus far been studied by Crighton [5], Morris [6], Ho and Gutmark [7], Hussain and Husain [8], and Husain and Hussain [9,10]. Elliptic jets issuing from sharp-edged orifii have been studied by Quinn [11], Hussain and Husain [8], Lee and Baek [12] and Yoon and Lee [13]. The instability of the shear layers emanating from high aspect ratio elliptic nozzles was studied analytically by Crighton [5]. Morris [6] extended, in numerical form, the analysis done by Crighton [5] to low aspect ratio elliptic nozzle jet flows. Ho and Gutmark [7] provided the results of an instability analysis of the shear layers and time-averaged mean flow and turbulence data, acquired with hot-wire anemometry, for a turbulent elliptic jet issuing from a contoured nozzle of aspect ratio 2. In addition, flow visualization results showed the streamwise evolution and deformation of the elliptic vortex rings shed at the nozzle exit plane. The experimental study of Hussain and Husain [8] produced time-averaged, frequency-domain and flow visualization data for unexcited (or unforced) and excited elliptic jets issuing from contoured nozzles of different small to moderate aspect ratios. Hot-wire anemometry was used to obtain the aforementioned time-averaged and frequency-domain data. This study also examined the effect of aspect ratio on elliptic free jets issuing from sharp-edged orifice plates. Husain and Hussain [9,10] extended their work reported in Hussain and Husain [8] to the study of elliptic jet coherent structures, using phase-averaging techniques. Time-averaged mean flow and turbulence data, acquired with hot-wire anemometry, for a turbulent issuing from a sharp-edged elliptic orifice plate of aspect ratio 5 were reported in the study of Quinn [11]. Lee and Baek [12] studied, using a laser Doppler velocimeter, the effect of aspect ratio on elliptic turbulent free jets issuing from sharp-edged orifice plates. The aspect ratio 2 jet was found to be the one with the best mixing characteristics among the jets (aspect ratio 1, 2, 4, 8) examined. Mean flow and turbulence data, obtained with stereoscopic particle imaging velocimetry, for a turbulent free jet issuing from a sharp-edged elliptic orifice of aspect ratio 2 were presented in the study of Yoon and Lee [13].

The present study was undertaken to provide a comprehensive set of time-domain mean flow, including the mean static pressure, and turbulence data and frequency-domain and phase-averaged turbulence data for a turbulent free jet issuing from a sharp-edged elliptic orifice plate. Such a study will contribute to a better understanding of the aforementioned better mixing characteristics of jets issuing from sharp-edged orifice plates compared with those from contoured nozzles. The aspect ratio of the orifice was chosen to be 2 so that meaningful comparisons can be made with the results of Ho and Gutmark [7], Hussain and Husain [8] and Husain and Hussain [9,10]. The results of the present study can also be used to facilitate the numerical computation of this flow.

2. Experimental details

2.1. The flow facility

The blow-down jet flow facility used in the present study is described in detail elsewhere (Quinn [3]). Very briefly, the flow facility consists of a small centrifugal fan, a diffuser, a settling chamber, a contraction and a screen cage. The fan, supported on anti-vibration neoprene pads, drew air from a room adjacent to the laboratory and delivered it to the sharp-edged elliptic orifice plate via the diffuser, settling chamber and contraction. The diffuser was fitted with a baffle at its upstream end, honeycomb and mesh-wire screens. The settling chamber was also fitted with mesh-wire screens. The three-dimensional contraction had a contour which is a third-degree polynomial that has zero derivatives as end conditions. The contraction had a circular cross-section at its upstream end and a square cross-section at its downstream end. The sharp-edged elliptic orifice plate, shown in Fig. 1, capped the downstream end of the contraction, which was flush with a plywood wall. The plywood wood wall ensured that entrainment of ambient fluid occurred only downstream of the orifice exit plane and not upstream. This also ensures that the mean streamwise velocity, U, is non-zero only at the orifice exit plane and zero everywhere else initially. The coordinate system used is shown in Fig. 1. The streamwise (X) coordinate is perpendicular to the spanwise (Y) and lateral (Z) coordinates and forms a right-hand system with them. The area contraction ratio was 283. The plywood wall formed one side of a screen cage which extended downstream from the wall. The experiments were performed in a large room.

A three-dimensional traversing system was used for moving the sensing probes in the flow field. The system consisted of a rack and pinion for traversing in the X direction and lead screws for traversing in the Y and Z directions.

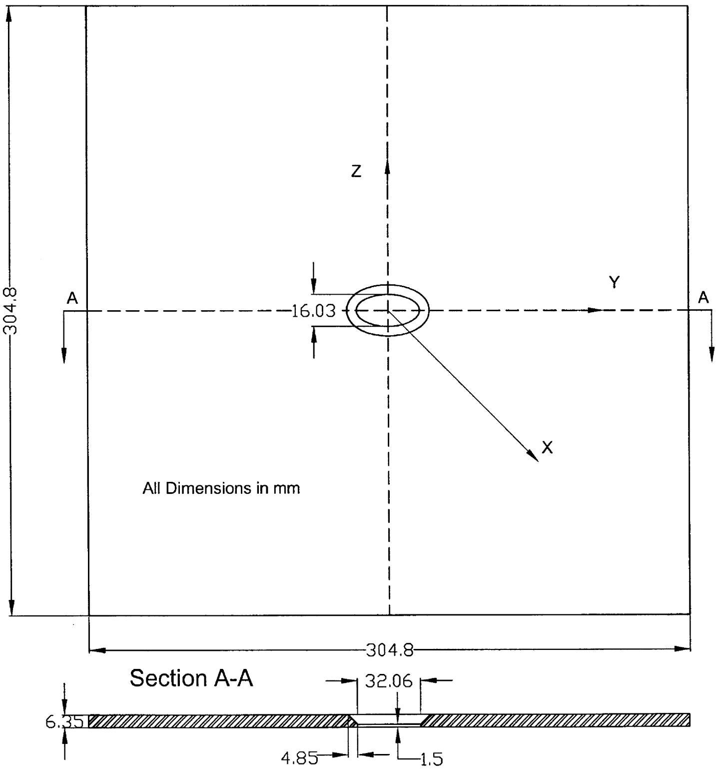

Fig. 1. Sharp-edged elliptic orifice plate.

The base of the traversing system was, like the fan, also supported on anti-vibration neoprene pads. Traversing in all three coordinate directions was effected by microcomputer-controlled stepping motors. Positioning accuracy of the sensing probes was 0.3 mm in the X direction and 0.01 mm in both the Y and Z directions. The data were acquired on a grid, in the Y–Z plane, at each X location. The grid spacing, which was kept the same in the Y and Z directions, varied from 2.54 mm close to the jet exit to 12.7 mm further downstream.

2.2. The flow diagnostics

The mean velocity and turbulence data were acquired with DANTEC P51 X-array probes. These probes consist of two 5 µm diameter platinum-plated tungsten slant wire sensing elements about 1 mm long and about 1 mm apart. The hot-wire probes, operated by DANTEC constant temperature anemometers at a resistance ratio of 1.8, were calibrated on-line close to the exit of the jet, where the mean streamwise velocity distribution in the central X–Y and X–Z planes was uniform and the corresponding streamwise turbulence intensity was low, against the output of a pitot-static tube which was connected to a pressure transducer and a Barocel electronic manometer. The calibration data were fitted to the exponent power law: $E^2 = A + BU_{\mathrm{eff}}^{\mathrm{n}}$ and A, B and n were optimized with a linear least-squares goodness-of-fit procedure. A “cosine law” response to yaw was assumed and the effective angle was found from a yaw calibration following Bradshaw [14]. Temperature variations from the calibration temperature were monitored with a thermocouple placed close to the hot-wire probe and corrections for such variations were made using the procedure in Bearman [15] in the data-reduction software. The mean flow and turbulence data were corrected for the effects of the mean velocity gradients on the spacing between the two slant sensing-wire elements of the X-array probes using the formulae given in Bell and Mehta [16]. The measurement of all the three components of the mean velocity vector with the X-array probes involved operating the probes in two positions, with the wires in the X–Y plane in one position and with the wires in the X–Z plane in the other position. This produced two sets of insignificantly different values of the U-component of the mean velocity vector. The insignificant difference in the U values obtained from measurements in the two previously mentioned positions implied that the wires were well matched and that ignoring the effect of the out-of-plane velocity (the so called transverse contamination) was appropriate here. Correction schemes such as those proposed by Clausen and Wood [17] for the components of the mean velocity and by Müller [18] for the turbulent stresses, were therefore, not used in the present study.

The hot-wire signals were linearized by the data reduction software and digitized, along with the signals from the thermocouple, with the National Instruments AT-A2150 dynamic signal acquisition board. This board consists of 4 analog input channels, each of 16-bit resolution. Each of the analog input channels is preceded by a third-order Butterworth low-pass analog anti-aliasing filter with an 80 kHz cut off. The filtered signal is sampled with a 1-bit delta-sigma modulating analog sampler at 64 times the chosen sampling rate. This reduces the quantization noise considerably. The output of the sampler is then fed to a digital anti-aliasing filter, which is built into the A/D converter chip, and the output of this filter re-samples the signal to the data rate, namely, 16-bit digital samples. It should be noted that all 4 analog input channels can be sampled simultaneously and, therefore, sample-and-hold units, which are required for successive approximation and dual slope A/D converters, are not needed here. The input range of the AT-A2150 board is ±2.828 volts (or 2 volts rms) so amplification was only needed for the thermocouple signal and not for the hot-wire signals. The mean velocity and turbulence data were obtained from records containing 8192 samples obtained at a sampling rate of 4 kHz.

The mean static pressure measurements were made with 2.3 mm diameter pitot-static tube, made of stainless steel with an ellipsoidal head and four circumferentially located static pressure holes, connected to a DATAMETRICS pressure transducer and an electronic manometer. These signals were also digitized with the AT-A2150 board but a voltage divider was needed to bring the signals into the input range of the board.

3. The initial conditions

The results of the mean velocity and turbulence measurements along the major and minor axes of the sharp-edged orifice plate at the exit plane are shown in Figs. 2 and 3, respectively. V and W are, respectively, the mean spanwise and mean lateral velocity. $\sqrt{\overline{u'^2}}/U_{\mathrm{cl}}$, $\sqrt{\overline{v'^2}}/U_{\mathrm{cl}}$ and $\sqrt{\overline{w'^2}}/U_{\mathrm{cl}}$ are the streamwise turbulence intensity, spanwise turbulence intensity and the lateral turbulence intensity, respectively, and U_{cl} is the value of U on the jet centerline. The mean streamwise velocity distribution along both axes of symmetry is typical of a jet issuing from a sharp-edged orifice, namely, U overshoots its value at the center as the sides of the orifice are approached. The turbulence intensities are low in the central portion of the jet, as expected since the mean streamwise velocity is nearly uniform there, and increase towards the sides due to the presence of shear layers in that region of the flow. The values for U and the turbulence intensities on the jet centerline at the orifice exit plane are as follows:

$$U = 62.4\ \mathrm{m/sec},$$
$$\sqrt{\overline{u'^2}}/U_{\mathrm{cl}} = 0.36\%,$$
$$\sqrt{\overline{v'^2}}/U_{\mathrm{cl}} = 0.04\%,$$
$$\sqrt{\overline{w'^2}}/U_{\mathrm{cl}} = 0.03\%.$$

The value of $U = 62.4\ \mathrm{m/sec}$ results in a Reynolds number, based on the equivalent diameter, $D_{\mathrm{e}} = 0.0453$ m, of the orifice, of 1.88×10^5. It should be noted that D_{e} is the diameter of a round orifice plate which has the same exit area as the elliptic orifice plate.

Both the V-velocities, shown in Fig. 2, and the W-velocities, shown in Fig. 3, are directed towards the centerline of the jet at the orifice exit plane. This is consistent with the vena contracta effect which is associated with jet flows issuing from sharp-edged orifice plates. Both of these secondary flow velocities have zero values on the jet centerline, as expected.

What appears to be a bias in the profiles of the measured quantities at the orifice exit plane, presented in Figs. 2 and 3, is really the result of trying to prevent the hot-wire sensors from hitting the edge of the orifice. Consequently, data points in either the y or the z direction are not symmetrically located on either side of the center of the orifice. Indeed contour maps of the measured quantities at locations downstream of the orifice exit plane, which will be presented subsequently, are reasonably symmetric.

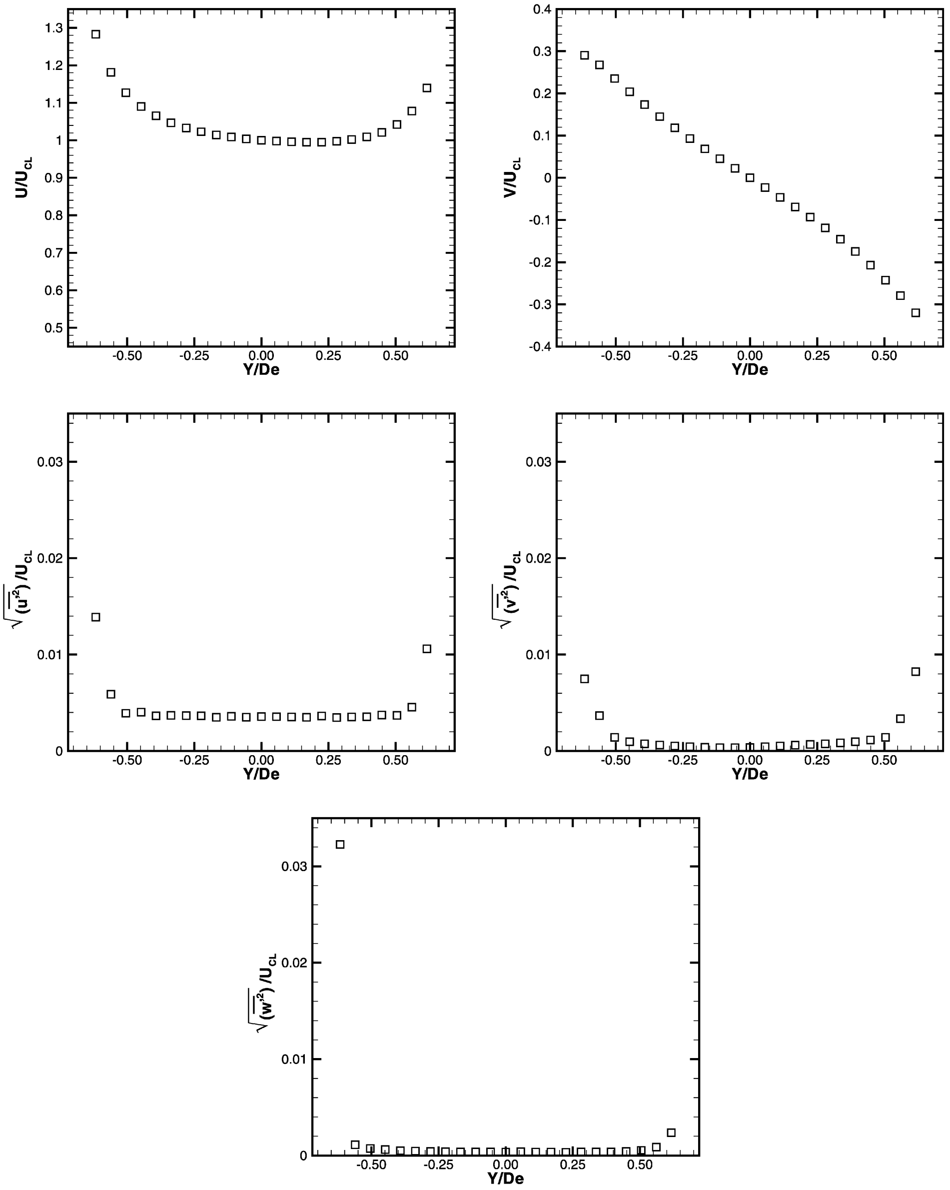

Fig. 2. Mean flow and turbulence intensity profiles along the major axis at the orifice exit plane.

The uncertainties in the measured data, all at 20:1 odds, which have been calculated using the method of Kline and McClintock [19], are as follows:

$$U \pm 1\%,$$
$$\overline{u'^2}, \overline{v'^2}, \overline{w'^2} \pm 6\%,$$
$$V, W \pm 3\%.$$

The odds in all the uncertainties in the measured data given subsequently will be the same, namely, 20:1, and will, therefore, not be restated.

The one-dimensional energy spectrum, $\phi_u(f)$, and the autocorrelation coefficient, $\rho_u(\tau)$, of the fluctuating streamwise velocity, u', and the probability density function of u' at the center of the slot exit plane are shown in Fig. 4. f is the frequency, $\sigma^2 = \overline{u'^2}$ here and τ is the time delay. Logarithmic ordinate and linear abscissa scales have been

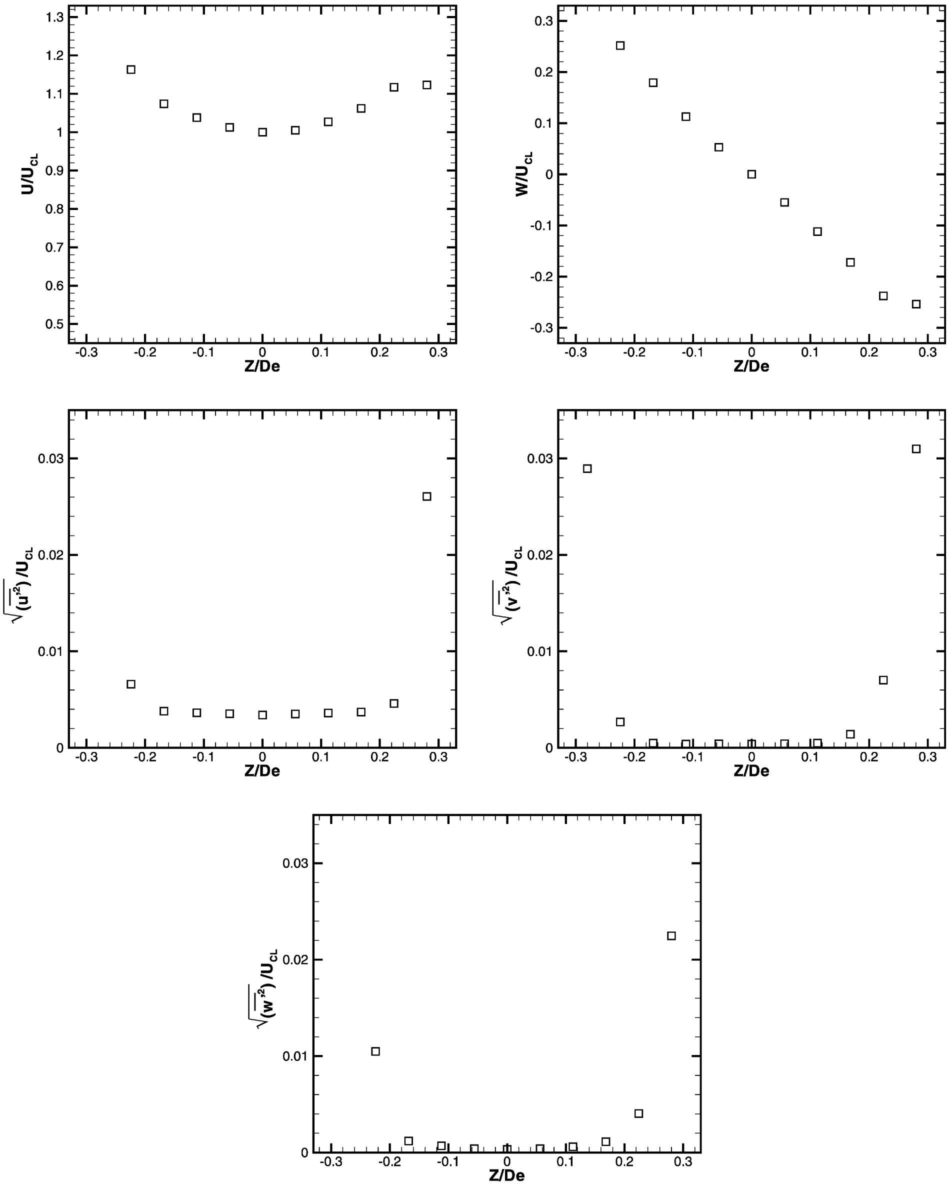

Fig. 3. Mean flow and turbulence intensity profiles along the minor axis at the orifice exit plane.

used to present the one-dimensional energy spectra here and in subsequent figures. The present unforced jet has a dominant peak in the frequency spectrum located at $f = 648.4$ Hz and resonant peaks at $f = 73.6$ Hz, 268.5 Hz and 394.0 Hz. The 648.4 Hz fundamental frequency results in a Strouhal number, based on the equivalent diameter of the sharp-edged orifice, of 0.47. By comparison, the Strouhal number, based on the nozzle width, in the unforced jet issuing from a sharp-edged rectangular slot, of aspect ratio 26.25, studied by Foss and Korschelt [20] was 0.43 and in the unforced round jet in the study of Crow and Champagne [21] the Strouhal number, based on the nozzle diameter, was 0.44. The periodic distribution of the autocorrelation coefficients is consistent with the presence of distinct peaks in the one-dimensional energy spectrum. The distribution of the probability density function of u' is consistent with the skewness factor,

$$S = \frac{\overline{u'^3}}{(\overline{u'^2})^{3/2}} = -0.658,$$

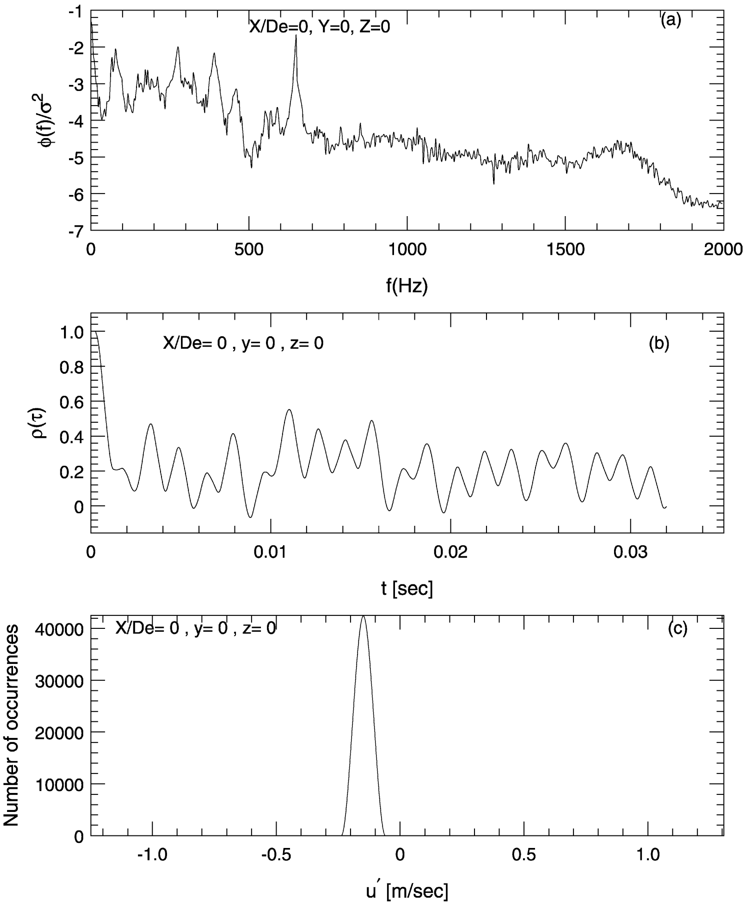

Fig. 4. One-dimensional energy spectrum, autocorrelation coefficient distribution of u' and the probability density function of U at the center of the orifice exit plane.

at this location in the flow. The probability density function of u' is therefore not centered on the mean value as in a Gaussian distribution.

4. Results and discussion

4.1. Mean streamwise velocity decay on the jet centerline

The decay of the mean streamwise velocity along the centerline of the present elliptic jet, which issues from a sharp-edged orifice plate, is shown in Fig. 5. The data, acquired in our laboratory, for round jets issuing from a sharp-edged orifice plate and from a contoured nozzle, and those of Ho and Gutmark [7] and Hussain and Husain [8] for elliptic jets issuing from contoured nozzles are included for comparison. It should be noted that the diameters of the sharp-edged round orifice plate and the contoured round nozzle were the same as the equivalent diameter of the sharp-edged elliptic orifice plate. The data of Hussain and Husain [8] were obtained at a Reynolds number, also based on the equivalent diameter of the nozzle, of 1×10^5 while those Ho and Gutmark [7] were acquired at a Reynolds number, based upon the length of the semi-major axis of the nozzle, of 0.78×10^5. The data of Ho and Gutmark [7], presented in terms of the semi-major axis of the nozzle as abscissa, have been converted so that the equivalent diameter of the nozzle becomes the abscissa for ease of comparison with the other data in Fig. 5. U_{exit} is the bulk-mean streamwise velocity at the exit plane of the sharp-edged orifice plate or nozzle. The results in Fig. 5 clearly show that the elliptic jet of the present study decays at a higher rate than the round jets and the contoured nozzle elliptic jets of Hussain and Husain [8] and Ho and Gutmark [7]. The lowest streamwise mean velocity decay rate is found in the contoured nozzle

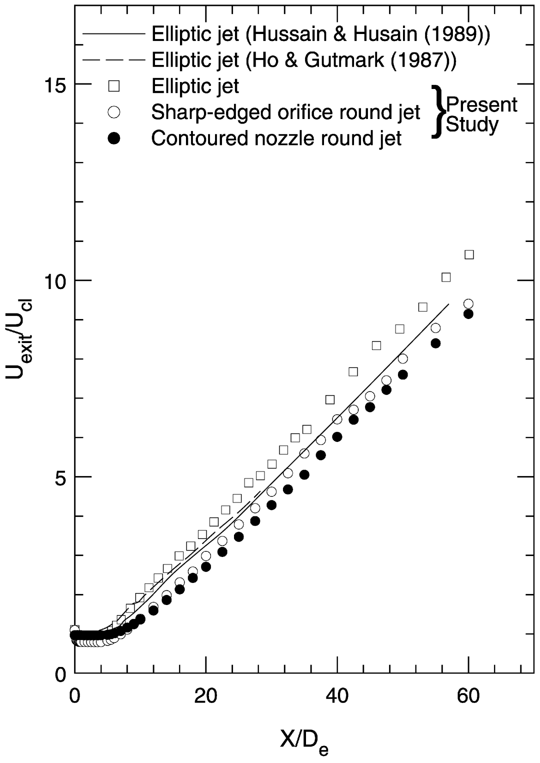

Fig. 5. Mean streamwise velocity decay on the jet centerline. The elliptic jets are of aspect ratio 2.

Table 1
Mean streamwise velocity decay rates and kinematic virtual origins

Jet	K_u	C_u	Range
Hussain and Husain [8]	0.164	−0.030	$15.4 \leqslant X/D_e \leqslant 57$
Ho and Gutmark [7]	0.151	3.530	$10.6 \leqslant X/D_e \leqslant 28.3$
Elliptic (present study)	0.184	0.426	$19.4 \leqslant X/D_e \leqslant 49.5$
Sharp-edged round orifice (present study)	0.167	−2.150	$18 \leqslant X/D_e \leqslant 55$
Contoured round nozzle (present study)	0.164	−3.650	$18 \leqslant X/D_e \leqslant 55$

elliptic jet of Ho and Gutmark [7] and this is most likely due to the fact that the measurement range, in terms of the equivalent diameter of the nozzle, is not as extensive as it is in the other jets. The potential core lengths of the elliptic jet, the sharp-edged round orifice plate jet and the contoured nozzle round jet of the present study are, respectively, 2.83 D_e, 3.50 D_e and 4.26 D_e, implying that near-field mixing among the three jets is highest in the elliptic jet. The data in Fig. 5 have been fitted by linear regression to:

$$U_{\mathrm{exit}}/U_{\mathrm{cl}} = K_u(X/D_e + C_u). \tag{4.1}$$

K_u is the mean streamwise velocity decay rate and C_u is the kinematic virtual origin.

The results are given in Table 1.

The data in Table 1 show that the mean streamwise velocity decay rates for the sharp-edged orifice plate jets are higher than those for the contoured nozzle jets implying, as has been observed by Quinn and Militzer [1], Mi et al. [2] and Quinn [3], higher mixing in the sharp-edged orifice plate jets than in the contoured nozzle jets. The kinematic virtual origins do not vary in any systematic manner. It is well known that the virtual origin of a jet is sensitive to initial conditions.

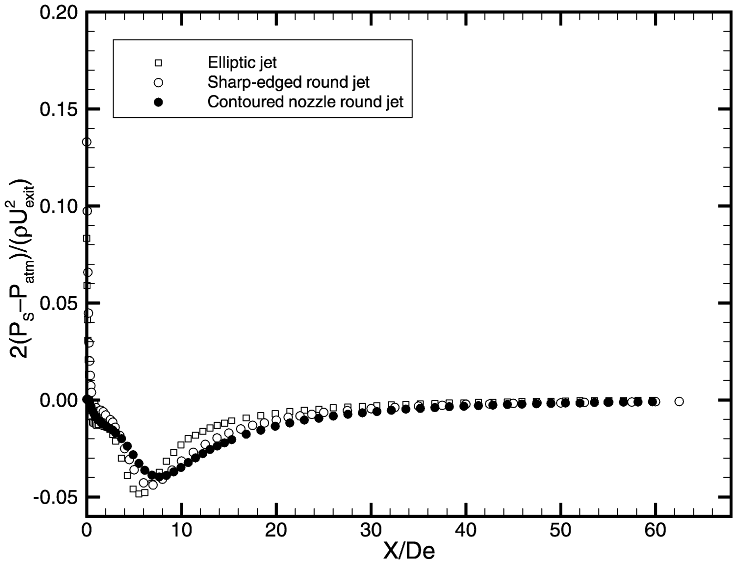

Fig. 6. Mean static pressure distribution on the jet centerline.

4.2. Mean static pressure distribution on the jet centerline

The mean static pressure distribution on the jet centerline for the elliptic jet is shown in Fig. 6. The uncertainty in the mean static pressure data is ±1%. The data for the round jets issuing from a sharp-edged orifice plate and from a contoured nozzle are included for comparison. P_s is the mean static pressure value anywhere on the jet centerline, P_{atm} is the atmospheric pressure, ρ is the density of the working fluid, air. The sharp-edged orifice plate jets exhibit similar behavior in the very near flow field, namely, the mean static pressure drops from a positive value (i.e., above atmospheric pressure) at the orifice exit plane to zero (i.e., atmospheric pressure) as a result of the acceleration of the jet fluid brought about by the vena contracta effect. The mean streamwise velocity data on the jet centerline, presented in Fig. 4, suggest that the acceleration of jet fluid ends at about $X/D_e = 0.5$. Note that the U_{exit}/U_{cl} values in Fig. 4 are less than one initially. The further decrease in the mean static pressure to negative values is triggered by the rapid production of turbulence from mean flow shear in the near flow field. The static pressure in the contoured nozzle round jet starts out at the atmospheric value and decreases to negative values as turbulence is produced, as stated previously, from mean flow shear. The centerline mean static pressure reaches its minimum at $X/D_e = 5.5$ in the elliptic jet compared to $X/D_e = 7.0$ in the sharp-edged orifice plate round jet and $X/D_e = 7.7$ in the contoured nozzle round jet.

4.3. Mean streamwise velocity contour maps

The contour maps for the mean streamwise velocity at several streamwise locations in the near field of the jet are shown in Fig. 7. Initially, at $X/D_e = 0.25$, the contours have the elliptic shape of the orifice and they are very closely spaced, indicating that very little mixing has taken place at this location. At the next two locations, $X/D_e = 0.75$ and 1.25, the contours still have an elliptic shape but are slightly wider spaced, implying that mixing is taking place. It is also observed at these two locations that the length of the major axis is gradually decreasing while that of the minor axis is correspondingly increasing. While both the V-velocities and W-velocities, it should be recalled, are directed towards the jet centerline at the orifice exit plane, the available data for these two quantities further downstream suggests that the V-velocities are directed towards the jet centerline while the W-velocities are directed away from the jet centerline. This results in a contraction of the mean streamwise velocity field along the major axis of the elliptic shape and in a corresponding expansion of this field along the minor axis of its elliptic shape. The mean streamwise velocity contour map is more or less circular at $X/D_e = 2.0$ and at $X/D_e = 3.0$ and beyond, the mean streamwise velocity field becomes elliptic again but the original minor and major axis now switched in orientation, a phenomenon which has been referred to as axis-switching. The reader interested in this phenomenon is referred to the review article by Gutmark and Grinstein [4].

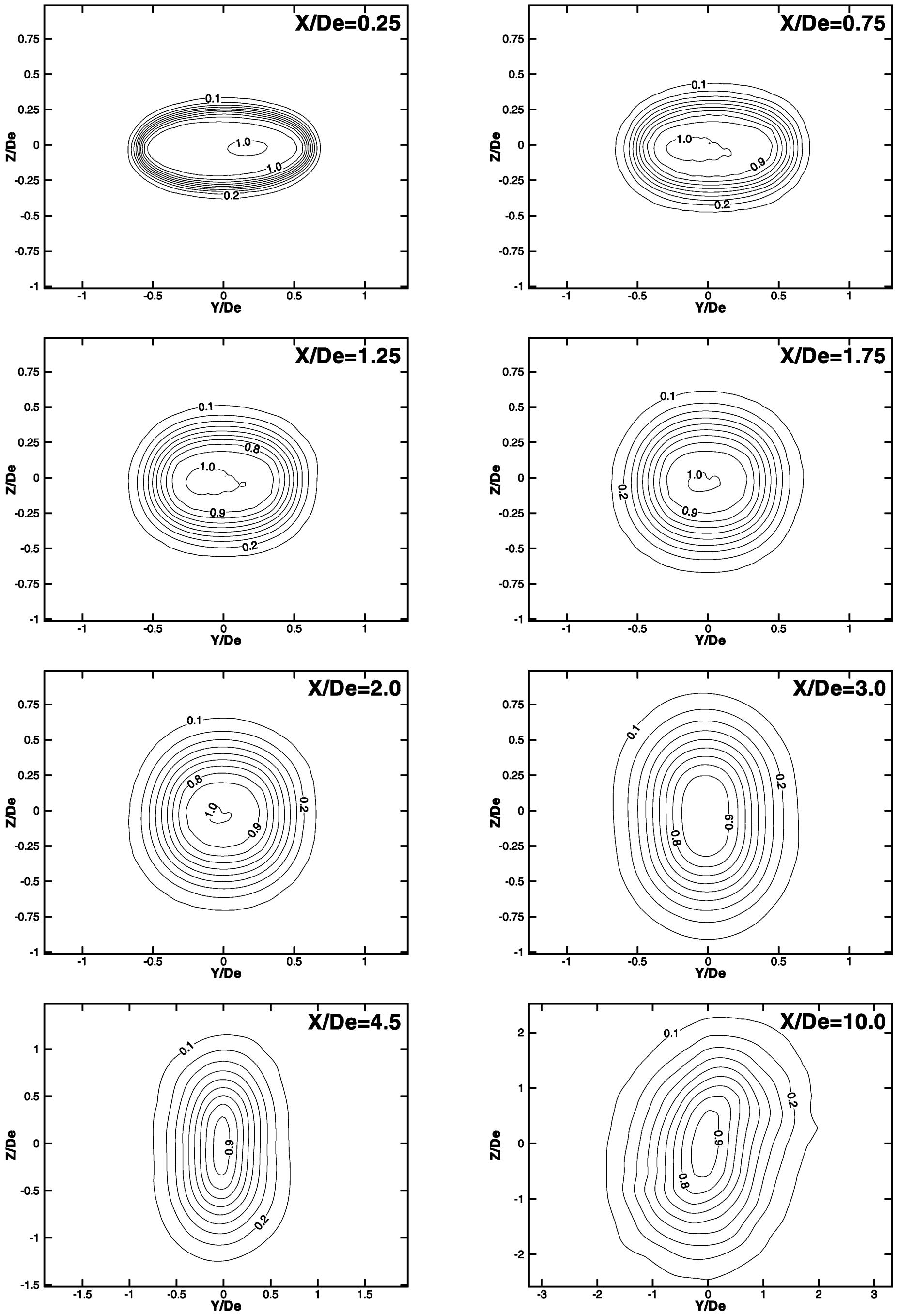

Fig. 7. Mean streamwise velocity (U/U_{cl}) contour maps.

4.4. Mass entrainment rates

Mass entrainment rates have been calculated from the mean streamwise velocity data by applying numerical quadrature to the relationship:

$$Q = \int_A \rho U \, \mathrm{d}A \tag{4.2}$$

and the results are shown in Fig. 8 for the sharp-edged orifice plate elliptic and round jets of the present study and for the elliptic jet of Ho and Gutmark [7] and the round jet of Hill [22]. Note that U in (4.2) is the absolute value. Q is the mass entrainment rate at any Y–Z plane in the flow, Q_o is the mass flow rate at the orifice or nozzle exit plane and dA is an elemental area on a Y–Z plane. The density of the fluid was taken as constant in the calculation. The mass entrainment rates in the elliptic jet are larger than those in the round jet of the present study and this difference in mass entrainment rates becomes significant with downstream distance. The higher mass entrainment rates in the elliptic jet imply enhanced mixing.

4.5. *Jet half-velocity widths*

The development of the jet half-velocity widths in the X–Y and X-Z planes, taken through the origin of the coordinate system in Fig. 1, is shown in Fig. 9 for the sharp- edged elliptic and round orifice plate jets of the present

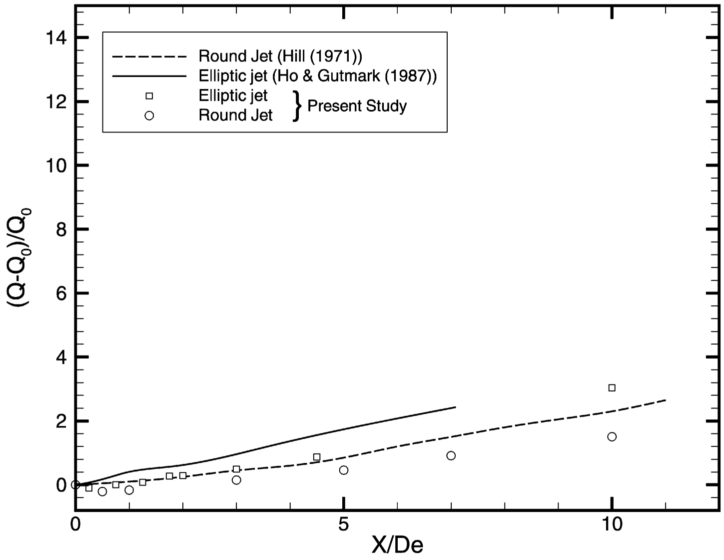

Fig. 8. Mass entrainment rates. The elliptic jets are of aspect ratio 2.

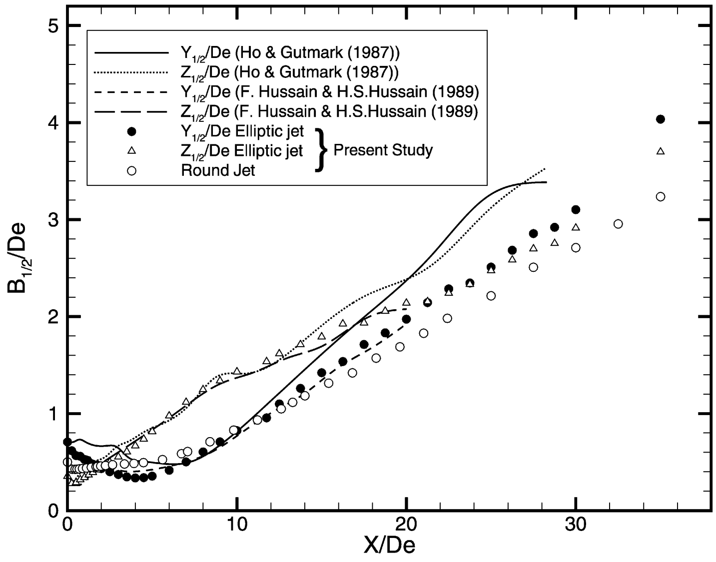

Fig. 9. Development of the jet half-velocity widths. The elliptic jets are of aspect ratio 2.

Table 2
Spreading rates and kinematic virtual origins

Jet	K_s	C_s	Range
Hussain and Husain [8]	0.1037	−0.0588	$8 \leqslant X/D_e \leqslant 22$
Ho and Gutmark [7]	0.1306	−0.2159	$7 \leqslant X/D_e \leqslant 22$
Elliptic jet (present study)	0.0972	0.1233	$10 \leqslant X/D_e \leqslant 20$
Sharp-edged round jet (present study)	0.0911	−0.0956	$10 \leqslant X/D_e \leqslant 22$

study. The results of Ho and Gutmark [7] and Hussain and Husain [8] are included for comparison. The half-velocity width of a jet is defined as the distance from the centerline of the jet to the point where the mean streamwise velocity is half its value on the jet centerline. $B_{1/2}$ is the general half-velocity width of the jet and $Y_{1/2}$ and $Z_{1/2}$ are the half-velocity widths in the central X–Y and X–Z planes, respectively. The half-velocity widths of the present elliptic jet and the elliptic jets of Ho and Gutmark [7] and Hussain and Husain [8] show similar behavior in both the X–Y and X–Z planes. In the X–Y plane, the half-velocity widths decrease initially and then increase monotonically with downstream distance while in the X–Z plane, the half-velocity widths increase monotonically except for the elliptic jet of the present study in which an initial decrease, due to the vena contracta effect, is observed. The behavior of the half-velocity widths is consistent with the evolution of elliptic vortex rings as observed in the flow visualization study of Gutmark and Ho [23]. This study showed that elliptic vortex rings, which are formed as a result of Kelvin-Helmholtz instability roll-up at the orifice or nozzle exit plane, shrink initially in the direction of the major axis before they start to grow in this direction and that the opposite behavior, namely, initial growth followed by shrinking, occurs in the direction of the minor axis. It appears that the deformation of such circumferential vortex rings, which is governed by the Biot–Savart law, controls entrainment into the jet, at least in the near flow field. The behavior of the half-velocity widths described above necessarily leads to a change in the orientation of the major and minor axes of the elliptic jets with downstream distance; this has been referred to as the axis-switching phenomenon in the extant literature, as mentioned previously. Two such axis switches, the first one at $X/D_e = 2.0$, which is in agreement with the results of Yoon and Lee [13], and the second one at $X/D_e = 24.0$, were found in the present elliptic jet. While there is some agreement among the results for the elliptic jets, the results of Hussain and Husain [8] are closer to those of the elliptic jet of the present study. All the elliptic jets spread at higher rates than the round jet, indicating enhanced mixing in the elliptic jets.

The geometric mean of the half-velocity widths, $B_e = (Y_{1/2}Z_{1/2})^{0.5}$, is used to facilitate a clearer comparison of the spread of the elliptic jets and the sharp-edged orifice plate round jet presented in Fig. 9. The data are shown in Fig. 10 from which it is clear, as noted previously, that the elliptic jets spread at a higher rate than the sharp-edged orifice plate round jet. The jet spread data in Fig. 10 have been fitted by linear regression to:

$$B_e/D_e = K_s(X/D_e + C_s) \tag{4.3}$$

K_s is the spreading rate and C_s is the geometric virtual origin. The results are shown in Table 2.

The difference in the spreading rates of the elliptic jets, especially between the elliptic jet of Ho and Gutmark [7] and that of Hussain and Husain [8], both of which issued from contoured nozzles, needs to be addressed. The difference in the nozzle geometry, i.e., sharp-edged orifice plate versus contoured nozzle can account for some of the difference in the spreading rates. While Hussain and Husain [8] reported a 2% variation of the initial momentum thickness in their aspect ratio 2 contoured nozzle jet flow, Ho and Gutmark [7] found a 26% variation of the initial momentum thickness in the jet issuing from a contoured nozzle also of aspect ratio 2. As it is well known, the initial momentum thickness of a jet plays an important role in the dynamics of coherent structures, which governs the spreading of the jet. Hence the difference in the spreading rates of the jets studied by Ho and Gutmark [7] and Hussain and Husain [8].

4.6. Mean static pressure contour maps

The mean static pressure contour maps are shown in Fig. 11. The mean static pressure distribution along the jet centerline presented in Fig. 6 for the elliptic jet showed positive values up to about $X/D_e = 1$ and negative values

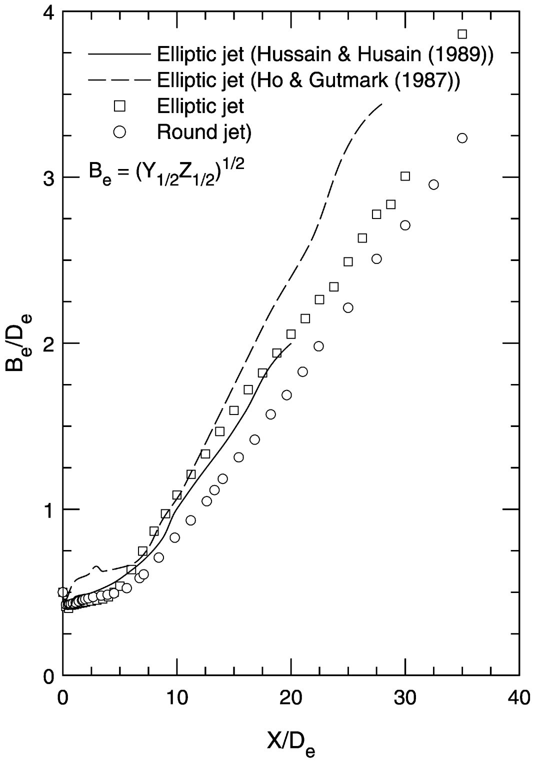

Fig. 10. Geometric mean of the jet half-velocity widths. The elliptic jets are of aspect ratio 2.

up to about $X/D_e = 20$. It is, therefore, not surprising to find positive mean static pressures in the central regions of the jet at $X/D_e = 0.25$ and 0.75 and negative mean static pressures throughout the jet at all the other measurement locations up to and including $X/D_e = 10.0$ in Fig. 11. It is clear that ambient fluid will generally be pumped into the jet as result of the difference in pressure between the ambient and the jet. This is the case from $X/D_e = 1.25$ onward. At the other two locations upstream of $X/D_e = 1.25$, regions of positive mean static pressure within the jet will pump jet fluid into those of negative mean static pressure. At $X/D_e = 0.25$, for example, jet fluid will be pumped from the positive mean static pressure "island" into the surrounding negative mean static pressure region which, in turn, will receive ambient fluid.

The assumption of quasi-steady, quasi-uniform and quasi-laminar flow around a pitot-static tube, implicit in the use of this sensing probe in turbulent shear flow, is strictly not valid in high intensity flow regions such as the shear layer regions of turbulent free jet flows like the elliptic jet of the present study. The resulting measurement error stems from the mean yaw and pitch angles of the velocity vector. Bradshaw and Goodman [24] and Christiansen and Bradshaw [25], however, have shown that the mean static pressure data acquired with pitot-static tubes of sizes frequently used in experimental work are probably close to the actual mean static pressure.

4.7. Mean streamwise vorticity contour maps

The mean streamwise vorticity, Ω_X, was calculated from the V- and W-velocity data by applying a central differencing procedure to the formula:

$$\Omega_X = \frac{\partial W}{\partial Y} - \frac{\partial V}{\partial Z} \tag{4.4}$$

and the results are shown as contour maps in Fig. 12. The uncertainty in the mean streamwise vorticity data is ±19.5%. Ω_X in the contour maps has been normalized by multiplying it by D_e and dividing the result by U_{cl}. Positive and

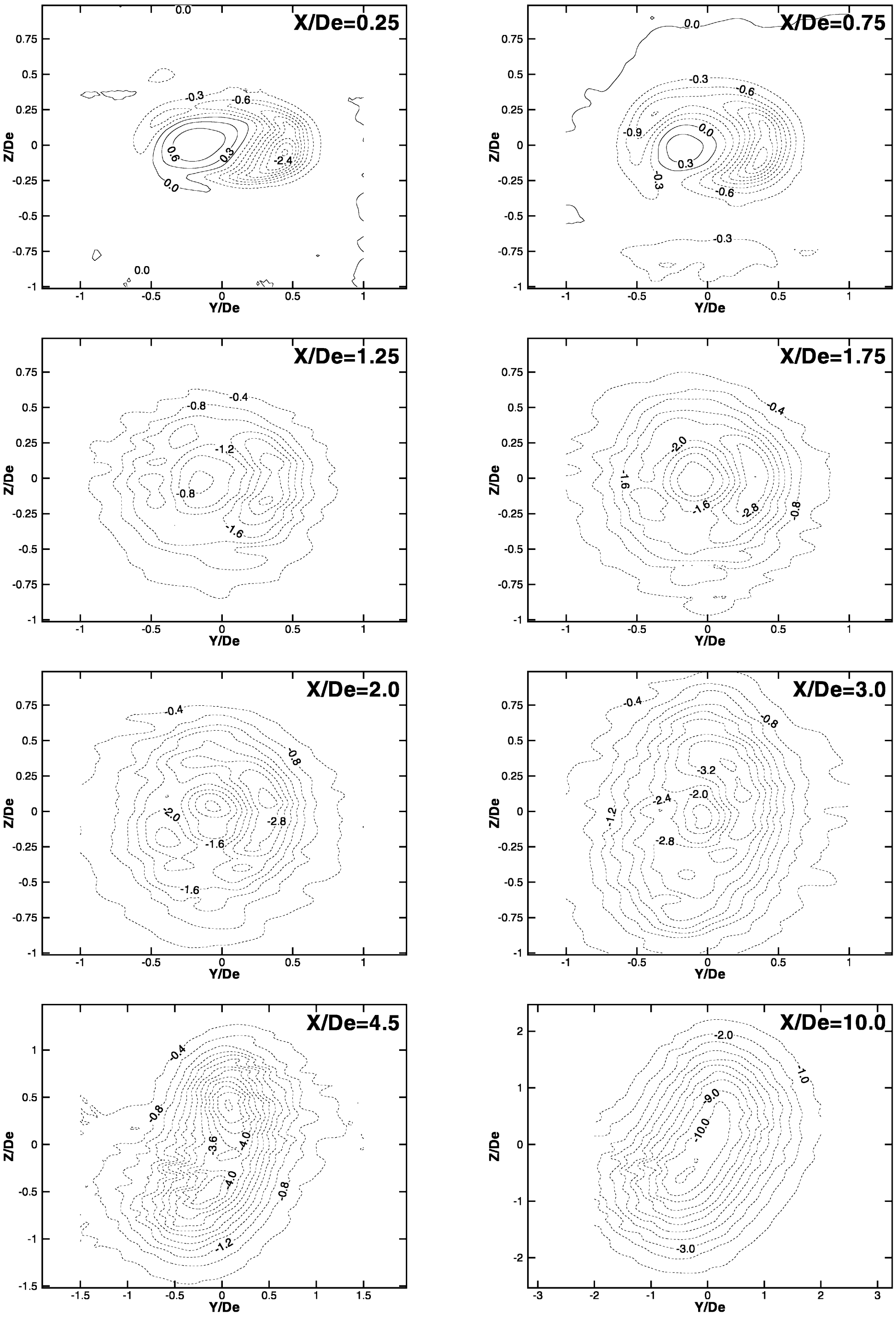

Fig. 11. Mean static pressure $(2(P_{\mathrm{s}} - P_{\mathrm{atm}})/(\rho U_{\mathrm{cl}}^2) \times 100)$ contour maps.

negative Ω_{x} indicate counter-clockwise and clockwise rotation, respectively, consistent with the right-hand system used here.

The transport equation for the mean streamwise vorticity is the analytical framework for discussing the mean streamwise vorticity contour maps. For the present steady, incompressible flow, this equation (see, e.g., Bradshaw [26], Perkins [27]) is as follows:

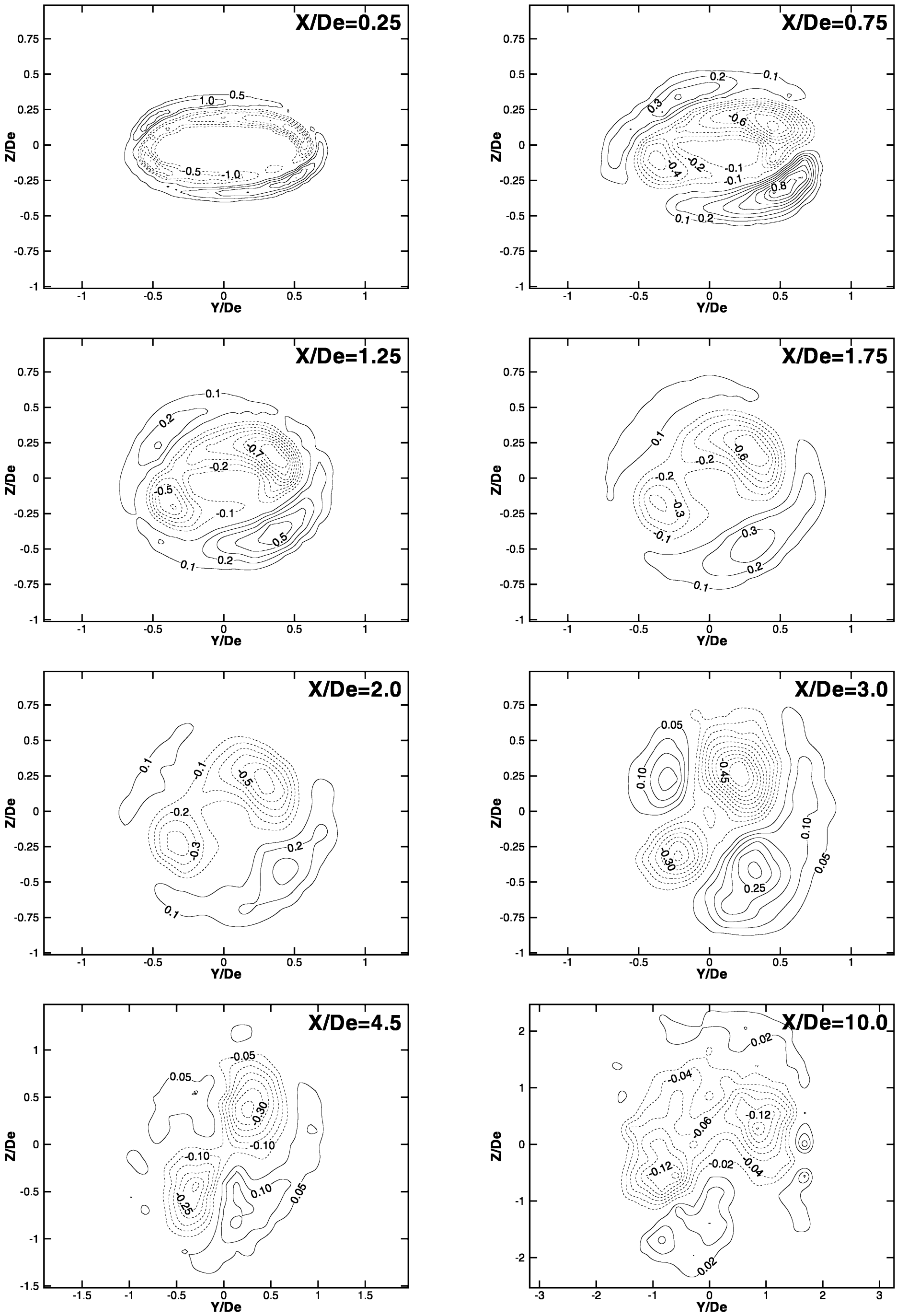

Fig. 12. Mean streamwise vorticity ($\Omega_X D_\mathrm{e}/U_\mathrm{cl}$) contour maps.

$$U\frac{\partial \Omega_X}{\partial X}+V\frac{\partial \Omega_X}{\partial Y}+W\frac{\partial \Omega_X}{\partial Z}=\Omega_X\frac{\partial U}{\partial X}+\Omega_Y\frac{\partial U}{\partial Y}+\Omega_Z\frac{\partial U}{\partial Z}+\frac{\partial^2}{\partial Y\partial Z}\left(\overline{v'^2}-\overline{w'^2}\right)$$
$$+\left(\frac{\partial^2}{\partial Y^2}-\frac{\partial^2}{\partial Z^2}\right)\overline{v'w'}+\nu\left(\frac{\partial^2\Omega_X}{\partial X^2}+\frac{\partial^2\Omega_X}{\partial Y^2}+\frac{\partial^2\Omega_X}{\partial Z^2}\right). \tag{4.5}$$

The three terms on the left-hand side of (4.5) represent the convection of the mean streamwise vorticity by the mean flow. The first three terms on the right-hand side of (4.5), which are referred to as Prandtl's secondary flow of the first kind, are the vorticity/velocity-gradient interaction which accounts for the exchange of vorticity between the different components through stretching (or contraction) ($\Omega_X \partial U/\partial X$) by the streamwise local shear in the mean streamwise velocity and tilting (or reorientation) ($\Omega_Y \partial U/\partial Y$, $\Omega_Z \partial U/\partial Z$) of the mean spanwise ($\Omega_Y$) and mean lateral ($\Omega_Z$) vorticity, respectively, by the spanwise and lateral local shear in the mean streamwise velocity. The fourth and fifth terms on the right-hand side of (4.5), which are also known as Prandtl's secondary flow of the second kind, represent the production of mean streamwise vorticity from gradients in the Reynolds normal stresses (or the turbulence anisotropy) and in the Reynolds secondary shear stress ($\overline{v'w'}$), respectively. The last three terms on the right-hand side of (4.5) represent the destruction (or dissipation) of the mean streamwise vorticity by the action of the kinematic viscosity, ν, of the jet fluid. In a high Reynolds number turbulent flow, like the present one, the contribution of these last three terms will be negligible.

Prior to discussing the present mean streamwise vorticity results, it will be useful to examine the extant knowledge on the generation of mean streamwise vorticity in round jet flows, which are really aspect ratio one elliptic jet flows. The work of Raman, Rice and Reshotko [28], among others, has shown that the jet issuing from a round nozzle will be unstable and two modes of instability have been identified. The first mode is the axisymmetric (or varicose) mode which develops very close to the nozzle exit and results in vortical ring structures which are formed from the Kelvin–Helmholtz roll-up of the periodically shed cylindrical vortex sheets at the nozzle exit plane. Liepmann and Gharib [29] have shown that mean streamwise vorticity is generated, by redistribution of azimuthal vorticity, in the braid region between vortical ring structures as a result of three-dimensional (or secondary) instabilities. The second mode is the helical (or sinuous) mode which occurs at some distance, typically after the end of the potential core, downstream of the nozzle exit. Vortical ring structures are also formed as result of the helical instability mode but, unlike the symmetric ones formed in the axisymmetric instability mode, these vortical ring structures are tilted.

As mentioned previously, vortical ring structures are also formed in an elliptic jet (Gutmark and Ho [23]). However, the induced velocity resulting from the variation of curvature around the elliptic contour triggers the deformation of the vortical ring structures so that these structures, unlike those in a round jet, do not remain in the plane normal to the flow direction. As it is in the case of round jets, it is reasonable to expect that mean streamwise vorticity will be generated in the braid region between the vortical ring structures in elliptic jets.

At $X/D_\mathrm{e} = 0.25$, the mean streamwise vorticity field consists of a pair of counter-rotating vortices. The mean streamwise vorticity field at all the other streamwise locations downstream of $X/D_\mathrm{e} = 0.25$ also have counter-rotating pairs of vortices but are tilted and compressed compared to the field at $X/D_\mathrm{e} = 0.25$. The tilting, which most likely stems from the reorientation of mean spanwise and lateral vorticity by $\partial U/\partial Y$ and $\partial U/\partial Z$, respectively, leads to a steeper inclined mean streamwise vorticity field with downstream distance and appears to lead to the well-documented axis-switching phenomenon. The compression of the mean streamwise vorticity field is probably due to negative values of $\partial U/\partial X$ since the acceleration of the fluid in the near flow field due to the vena contracta effect, as mentioned previously, ends at about $X/D_\mathrm{e} = 1.0$. Gradients of the turbulence anisotropy and the Reynolds secondary shear stress will also contribute, as shown in (4.5) above, to the generation of mean streamwise vorticity in the present flow.

4.8. Evolution of the turbulence intensities along the jet centerline

The evolution of the streamwise ($\sqrt{\overline{u'^2}}/U_\mathrm{exit}$), spanwise ($\sqrt{\overline{v'^2}}/U_\mathrm{exit}$), and lateral ($\sqrt{\overline{w'^2}}/U_\mathrm{exit}$) turbulence intensities along the jet centerline of the elliptic jet is shown in Fig. 13. For comparison, the jet centerline evolution of the streamwise and spanwise turbulence intensities for the jets issuing from the sharp-edged round orifice plate and the contoured round nozzle is shown in Fig. 14. A rapid increase in all the turbulence intensities is observed initially as turbulence, produced by mean flow shear in the shear layers, is transported by diffusion to the jet centerline. The turbulence intensities in the elliptic jet peak (with $\sqrt{\overline{u'^2}}/U_\mathrm{exit} \cong 19.3\%$) at $X/D_\mathrm{e} = 6.4$ before the turbulence intensities in the sharp-edged round orifice plate and contoured nozzle round jets reach their peak values at $X/D_\mathrm{e} = 8.0$ and $X/D_\mathrm{e} = 9.0$, respectively, indicating enhanced mixing in the elliptic jet. It should be recalled that the mean static pressure along the jet centerline in the elliptic jet, shown in Fig. 6, also starts to recover from negative values towards atmospheric pressure before the mean static pressure in the round jets do. In the aspect ratio 2 sharp-edged elliptic orifice jet studied by Hussain and Husain [8], the peak $\sqrt{\overline{u'^2}}/U_\mathrm{exit}$ value of about 22% occurred at $X/D_\mathrm{e} = 6.92$.

The root-mean-square values of the fluctuating velocities along the jet centerline are usually normalized by the local mean streamwise velocity. The resulting turbulence intensity, plotted against X/D_e, is presented in Fig. 15 for

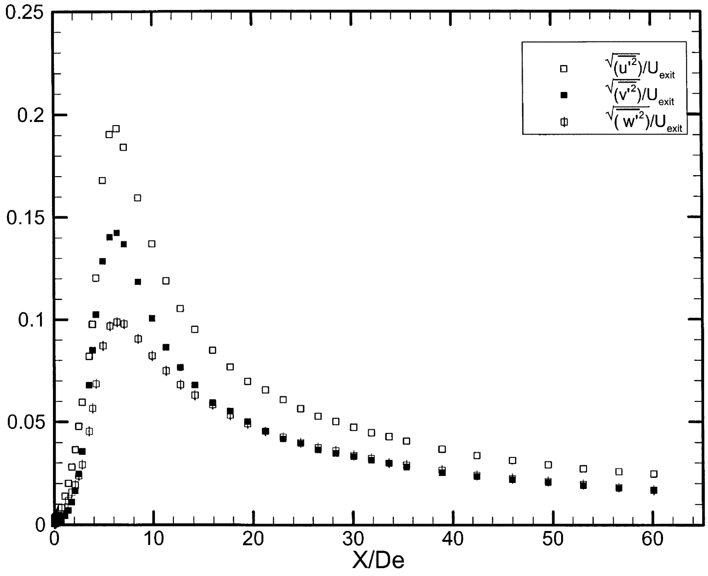

Fig. 13. Evolution of the turbulence intensities on the jet centerline of the elliptic jet.

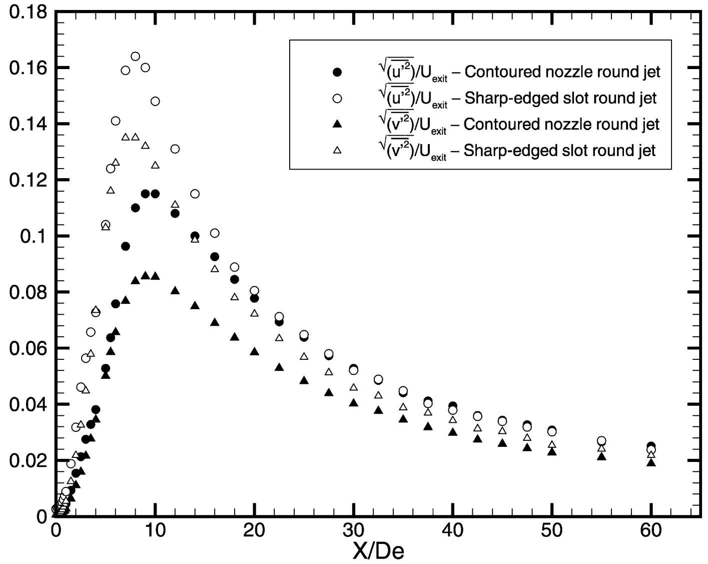

Fig. 14. Evolution of the turbulence intensities on the jet centerline for the sharp edged orifice plate and contoured nozzle round jets.

the present elliptic jet along with the results for the sharp-edged round orifice plate jet and those of Hussain and Husain [8] for an elliptic jet issuing from a contoured nozzle of aspect ratio 2. The behavior of the turbulence intensities on the jet centerline is as described previously except that significantly higher values are found especially in the far field, because of the decreasing local streamwise velocities.

As it is well known, the local turbulence intensities in all free jet flows issuing into a still ambient increase with distance from the jet centerline in a monotonic fashion and reach high values (in excess of 50%) towards the edge of the jet where the local mean streamwise velocity is low. The interpretation of hot-wire signals becomes quite uncertain when the local turbulence intensity exceeds 30% due to flow reversals, as has been mentioned by Bradshaw [14]. This will in general lead to an overestimation of the mean velocity and an underestimation of the double correlation turbulence quantities in such high local turbulence intensity regions of free jets and the reader is urged to treat the data in these regions of the flow with caution. However, the study of Browne, Antonia and Chua [30] has shown that the

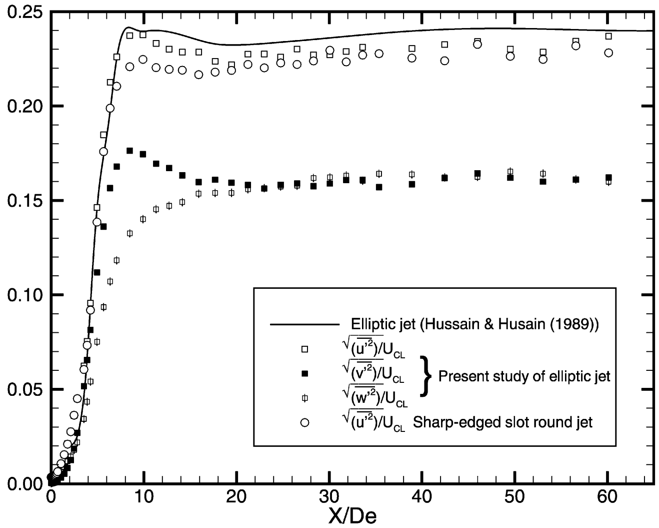

Fig. 15. Variation of the turbulence intensities on the jet centerline.

data for the Reynolds streamwise normal stress and the Reynolds primary shear stresses, acquired using the effective angle yaw calibration method such as the one used in the present study, are far less affected by local high turbulence intensity effects than the Reynolds spanwise and lateral normal stresses.

4.9. The Reynolds normal stress contour maps

Contour maps for the streamwise Reynolds normal stress ($\overline{u'^2}$), normalized by U_{cl}^2 and amplified by a factor of 100, are shown in Fig. 16. The shapes of these contour maps correspond very closely to those of the mean streamwise velocity shown in Fig. 7 at the corresponding streamwise locations. Large or small values of the streamwise Reynolds normal stress are found, as is to be expected and as will be shown later, in regions where the local shear in the mean streamwise velocity ($\partial U/\partial Y$, $\partial U/\partial Z$) is large or small. Indeed, taking the thin shear layer approximation into consideration, the production of the streamwise Reynolds normal stress is given by:

$$P\left(\overline{u'^2}\right) = \left(-\overline{u'v'}\right)\frac{\partial U}{\partial Y} + \left(-\overline{u'w'}\right)\frac{\partial U}{\partial Z} \tag{4.6}$$

where $\overline{u'v'}$ and $\overline{u'w'}$ are the spanwise and lateral Reynolds primary shear stresses, respectively. The close relationship between $\overline{u'^2}$ and $\partial U/\partial Y$, $\partial U/\partial Z$ is clearly seen in (4.6).

The data for the spanwise ($\overline{v'^2}$) and lateral ($\overline{w'^2}$) Reynolds normal stresses, which are not presented here, show behavior similar to that described in Fig. 16 for the streamwise Reynolds normal stress at the corresponding locations in the flow field. Unlike the streamwise normal stress, which is produced directly from the local shear in the mean streamwise velocity as (4.6) shows, the spanwise and lateral Reynolds stresses are not obtained from the mean flow local shear but from the streamwise Reynolds normal stresses via the pressure fluctuations.

4.10. The Reynolds primary shear stress contour maps

The spanwise Reynolds primary shear stress ($\overline{u'v'}$ or, strictly, $\rho\overline{u'v'}$), normalized by U_{cl}^2 and amplified by 100, contour maps are shown in Fig. 17. The uncertainty in the Reynolds primary shear stress data is ±8%. The spanwise Reynolds primary shear stress represents the mean rate of transfer of the spanwise component of the linear momentum through a unit area normal to the streamwise direction. Contour maps for the local spanwise shear ($\partial U/\partial Y$) in the mean streamwise velocity are shown in Fig. 18 to facilitate the discussion of the spanwise Reynolds primary shear stress results. It is clear from Figs. 17 and 18 that the spanwise Reynolds primary shear stress is well correlated with the spanwise local shear in the mean streamwise velocity. This is not surprising since the dominant term in the generation of $\overline{u'v'}$ by the mean flow is $\overline{v'^2}\partial U/\partial Y$.

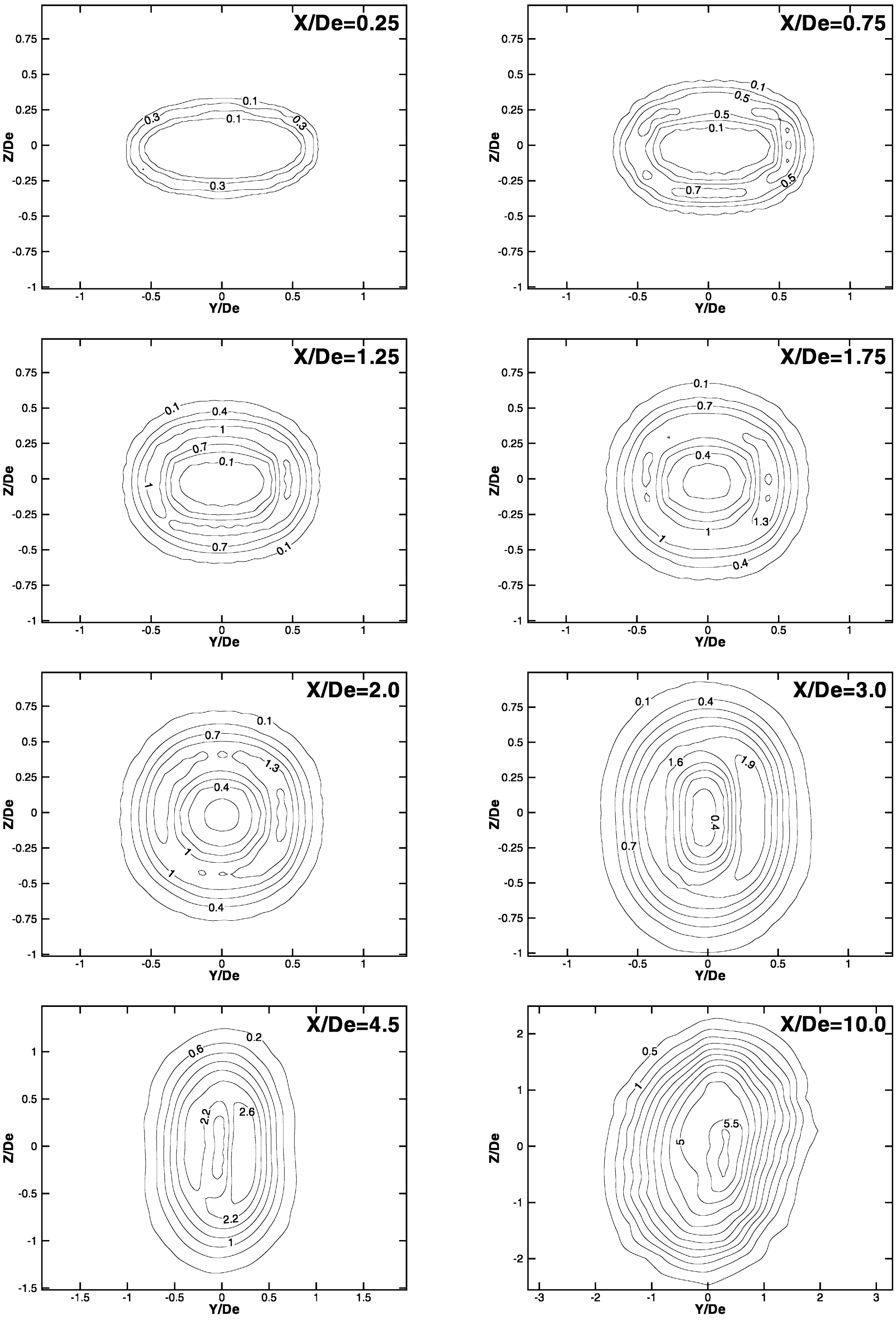

Fig. 16. Streamwise Reynolds normal stress ($\overline{u'^2}/U_{\mathrm{cl}}^2 \times 100$) contour maps.

The lateral Reynolds primary shear stress ($\overline{u'w'}$), normalized and amplified in the same way as was done with $\overline{u'v'}$, contour maps are shown in Fig. 19 and those for the local lateral shear ($\partial U/\partial Z$) in the mean streamwise velocity are shown in Fig. 20. The lateral Reynolds primary shear stress, which is produced from the mean flow mainly by the term $\overline{w'^2}\partial U/\partial Z$, is clearly well correlated with the lateral mean strain ($\partial U/\partial Z$) as was the case with the spanwise Reynolds primary shear stress data which were discussed previously.

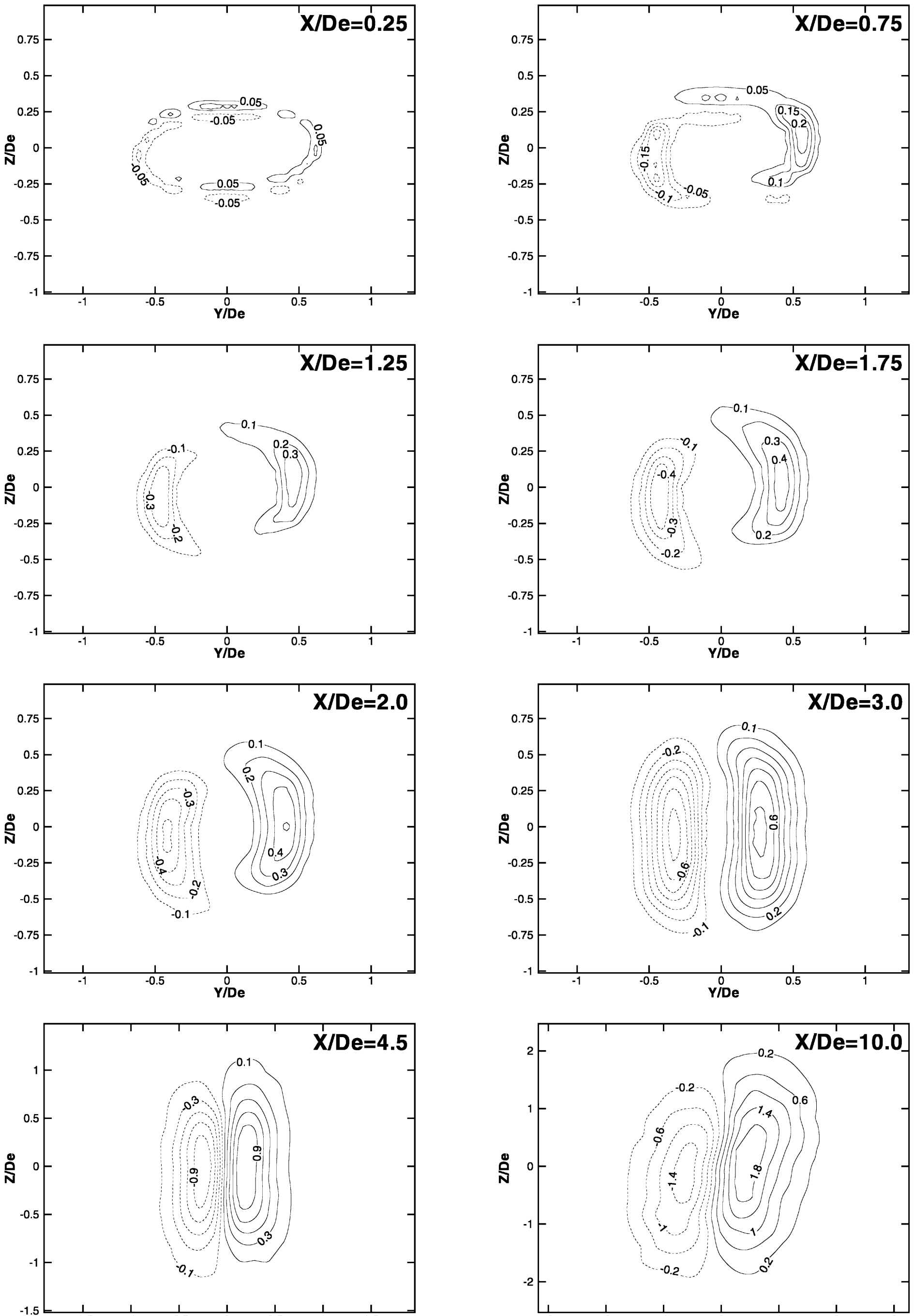

Fig. 17. Spanwise Reynolds primary shear stress ($(\overline{u'v'}/U_{\mathrm{cl}}^2) \times 100$) contour maps.

4.11. The distribution of autocorrelation coefficients of the streamwise fluctuating velocity on the jet centerline

The autocorrelation coefficient of the streamwise fluctuating velocity (u') is given by:

$$\rho_u(\tau) = \frac{\overline{u'(t)u'(t+\tau)}}{\overline{u'^2(t)}} \tag{4.7}$$

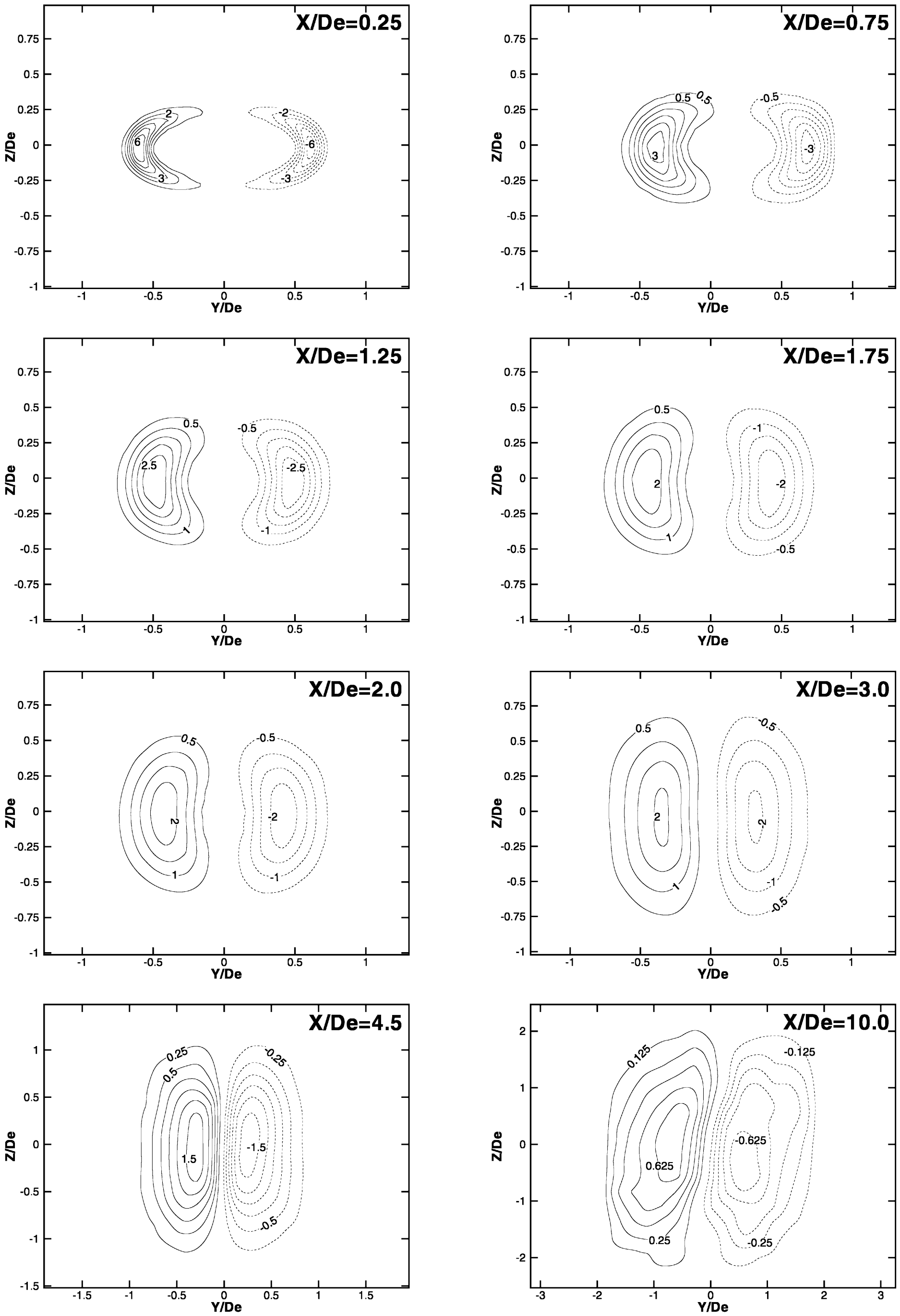

Fig. 18. Spanwise shear ($\partial U/\partial Y$) in the mean streamwise velocity contour maps.

where t and τ, are the time and time delay, respectively. The distribution of autocorrelation coefficients of u' at various locations on the jet centerline in the near field of the jet is shown in Fig. 21. The autocorrelation coefficients of the spanwise (v') and lateral (w') fluctuating velocities were also measured and their distribution at the same streamwise locations shown in Fig. 21 exhibited behavior similar to that of the distribution of the autocorrelation coefficients of the streamwise fluctuating velocity, which is yet to be discussed, and are, therefore, not presented here. The autocorrelation and power spectrum, being Fourier Transform pairs, are known to have an inverse spreading relationship. This

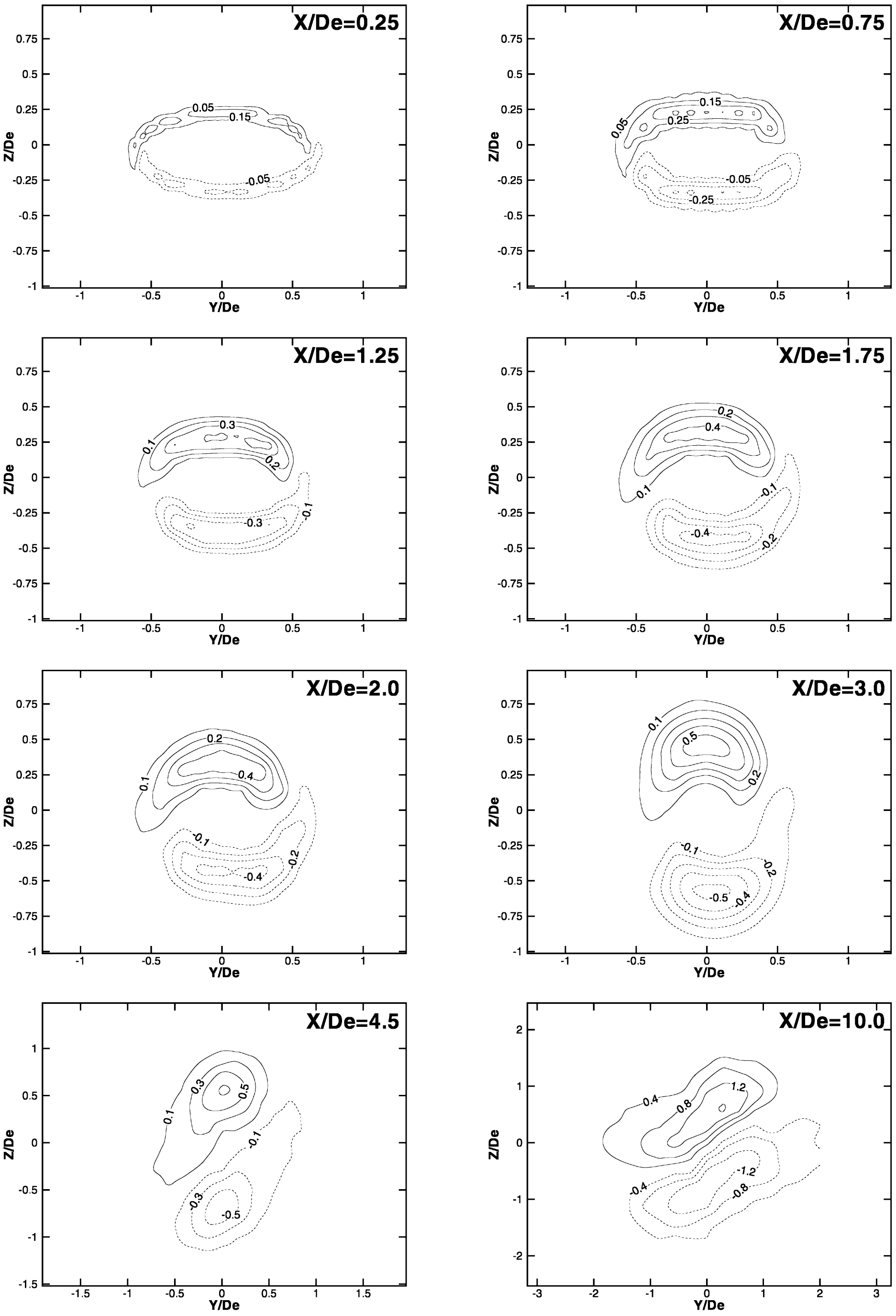

Fig. 19. Lateral Reynolds primary shear stress ($(\overline{u'w'}/U_{\mathrm{cl}}^2) \times 100$) contour maps.

means that if the power spectrum is very narrow, the distribution of the autocorrelation coefficients will oscillate with decreasing amplitude and with a frequency equal to that at which the peak in the power spectrum is centered as can be seen at all the locations shown in Fig. 21 except at $X/D_{\mathrm{e}} = 10.0$, where the autocorrelation coefficients distribution is broadband, implying fully turbulent flow at this location. The periodic distribution of the autocorrelation coefficients described above implies that the fluctuating signal has a coherent component. In anticipation of the discussion of the one-dimensional energy spectra of the streamwise fluctuating velocity, it should be noted that the inverse of the time,

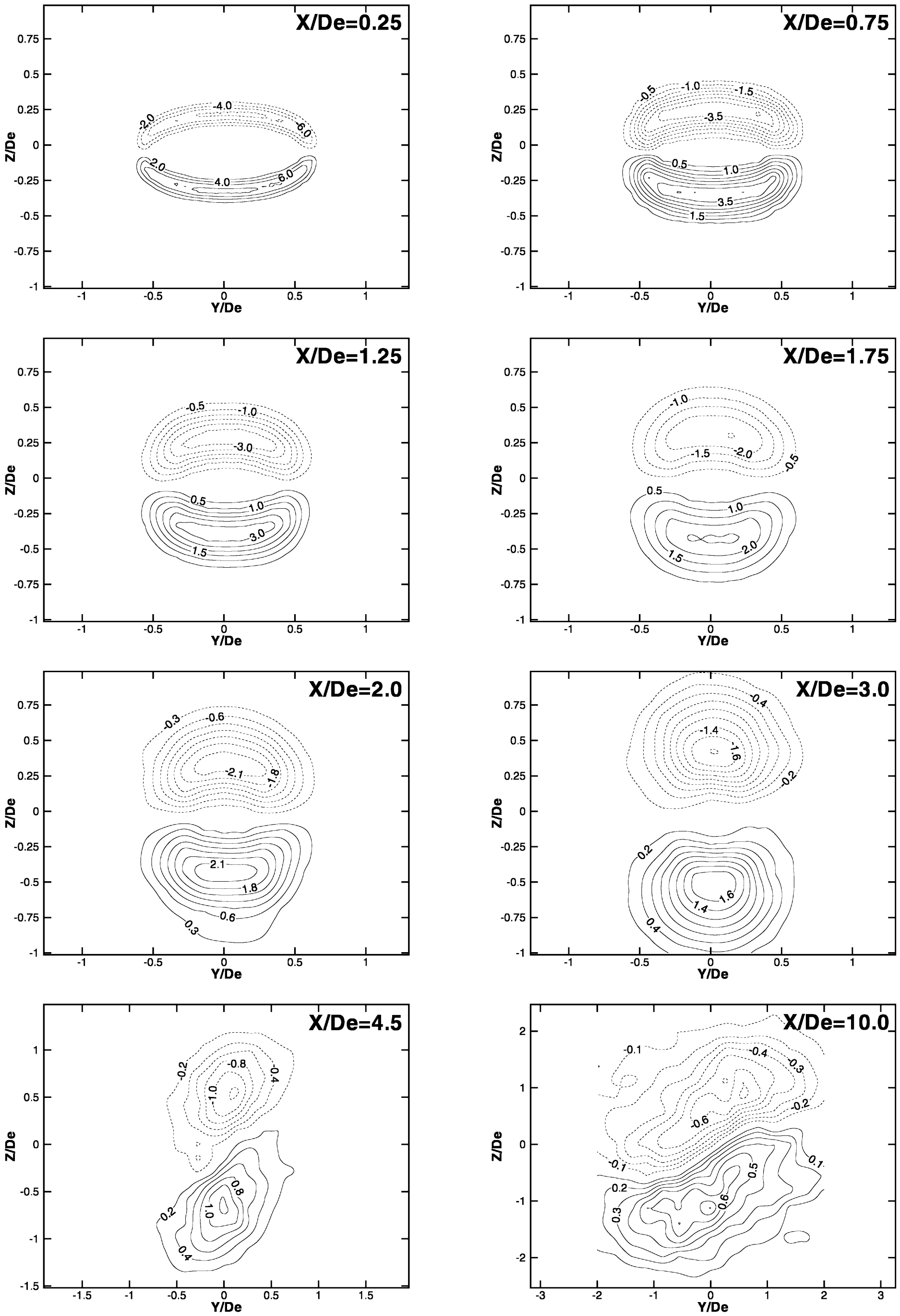

Fig. 20. Lateral shear ($\partial U/\partial Z$) in the mean streamwise velocity contour maps.

$t = 0.0015422$ seconds, at which the autocorrelation coefficients distribution has its second maximum is 648.4 Hz, which, it should be recalled, was the fundamental frequency of the flow at the orifice exit plane.

4.12. One-dimensional energy spectra of the streamwise fluctuating velocity on the jet centerline

The one-dimensional energy spectra of the streamwise fluctuating velocity at several streamwise locations on the jet centerline in the near flow field are shown in Fig. 22. The reader is reminded, as was already stated previously, that

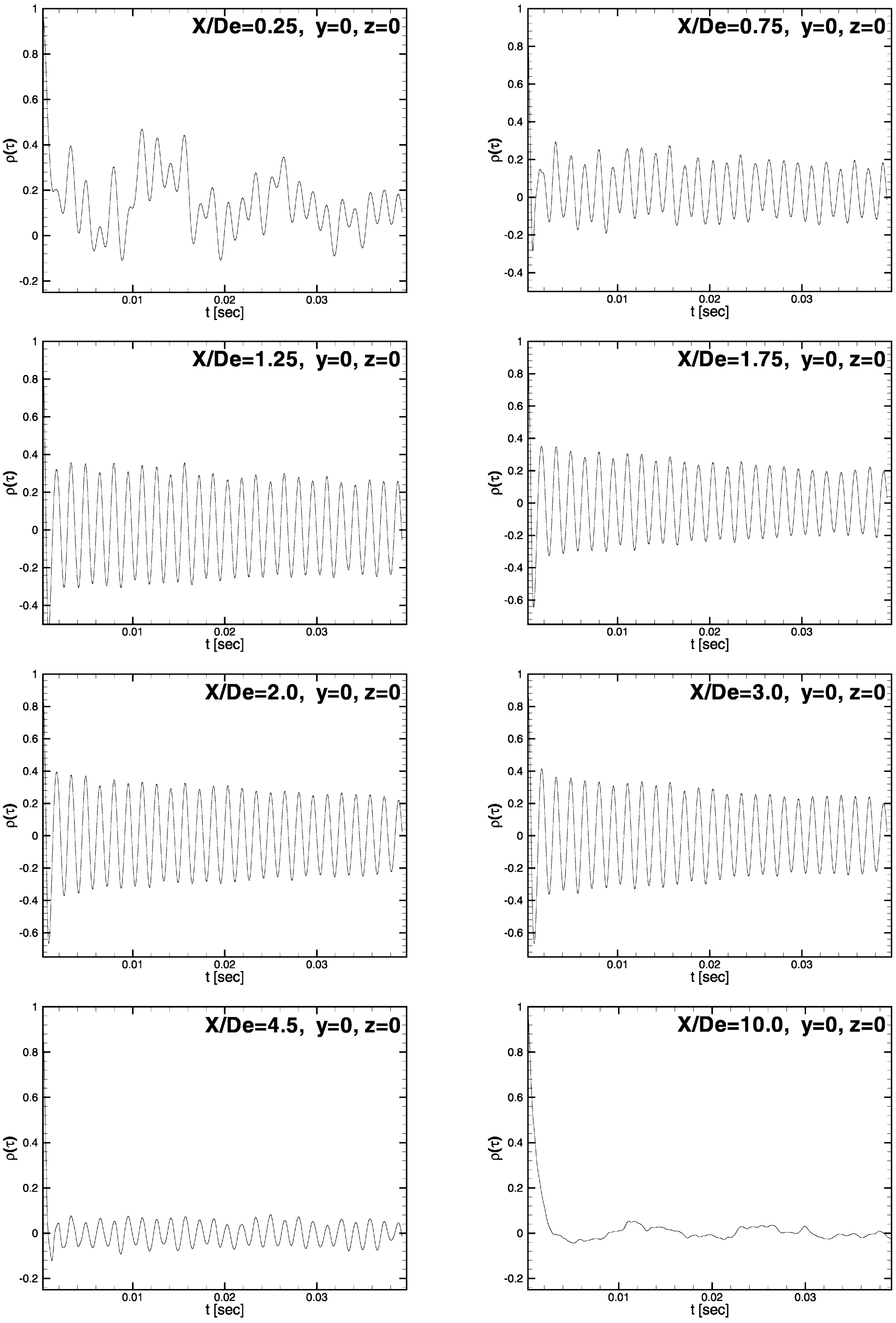

Fig. 21. Distribution of the autocorrelation coefficients for u' on the jet centerline.

the ordinate scale in Fig. 22 is logarithmic while the abscissa scale is linear. These one-dimensional energy spectra have been obtained from Fast Fourier Transforms (FFT) of the digital hot-wire time-series data. It can be shown, assuming that the data are statistically stationary, that:

$$\overline{u'^2} = \int_0^\infty \phi_u(f)\,\mathrm{d}f. \tag{4.8}$$

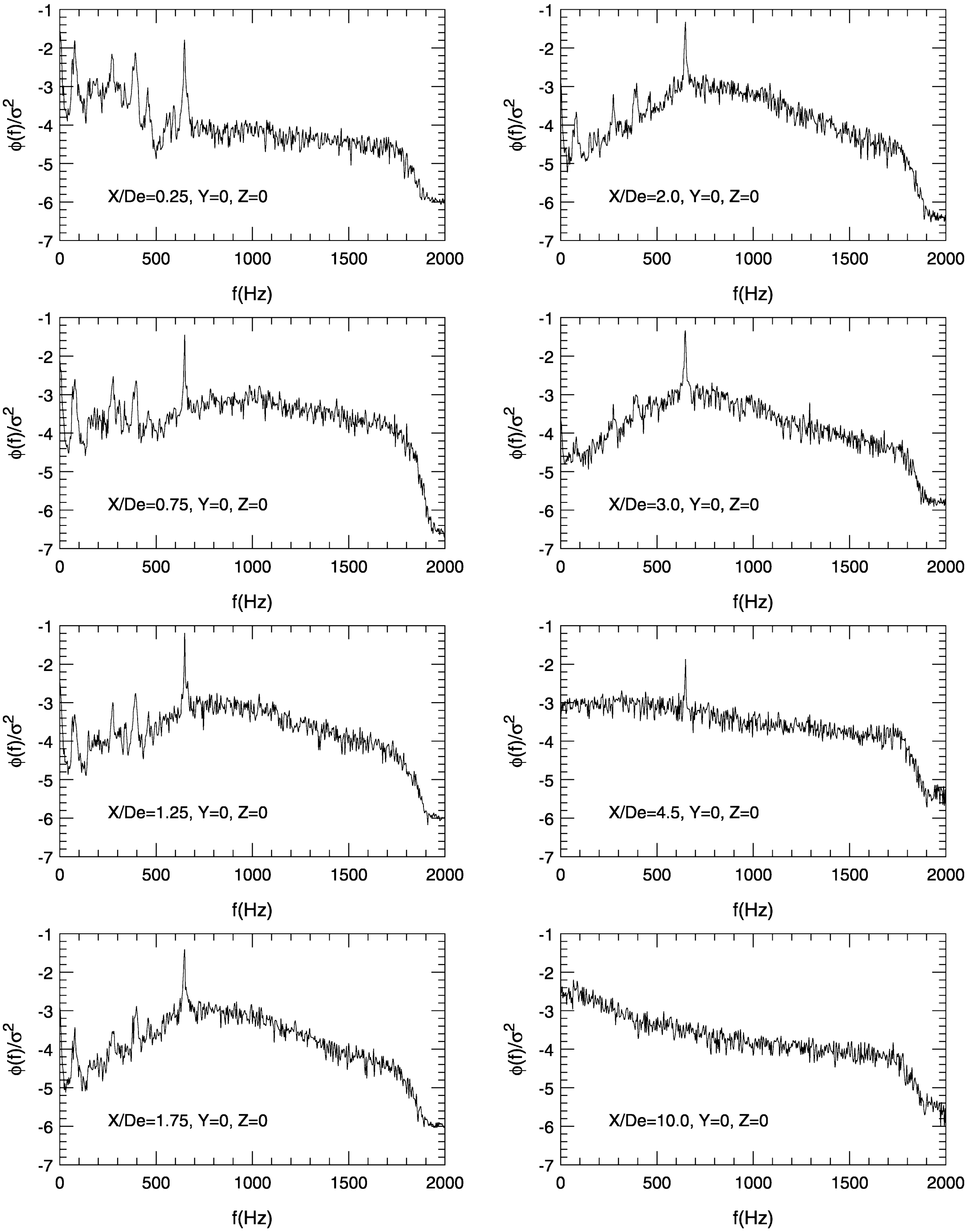

Fig. 22. One-dimensional energy spectra for u'on the jet centerline.

Therefore, at each location, the one-dimensional energy spectra have been normalized by $\overline{u'^2}$. The one-dimensional energy spectra exhibit, consistent with the autocorrelation coefficient distribution shown in Fig. 21, discrete peaks at a frequency of 648.4 Hz at all the locations shown in Fig. 22 except at $X/D_\mathrm{e} = 10.0$ where it is broadband and, as in fully developed turbulent flow, the large-scale coherent structure is masked by fine-scale turbulence. These discrete peaks in the one-dimensional energy spectra at a constant frequency of 648 Hz suggest global oscillations of the flow field that extend beyond the potential core of the jet. The constant Strouhal number of 0.47 implies, according to results of Ganesh, Rice and Reshotko [28], that the instability mode is axisymmetric initially and symmetric structures will exist in the jet shear layers at least up to $X/D_\mathrm{e} = 4.5$ in the present elliptic jet. The helical instability mode is known to occur at lower Strouhal numbers (see Ganesh, Rice and Reshotko [28]). The magnitude of the discrete peaks in the one-dimensional energy spectra varies with streamwise location but the largest magnitude occurs at $X/D_\mathrm{e} = 1.25$. The variation in the magnitude of discrete peaks in the one-dimensional energy spectra suggests that the flow oscillation amplitude is varying in the flow field. The one-dimensional energy spectra of the spanwise and lateral fluctuating velocities, which have also been obtained, behave in a manner similar to that of their streamwise counterpart and are, therefore, not presented here. The streamwise Reynolds normal stress, $\overline{u'^2}$, is most amplified, as Fig. 13 shows, at $X/D_\mathrm{e} = 6.4$ in the present elliptic jet and at $X/D_\mathrm{e} \cong 8$ in the unforced elliptic jet issuing from a contoured nozzle of aspect ratio 2 in the study of Hussain and Husain [8]. The corresponding Strouhal numbers, based on the equivalent diameter of the orifice or nozzle, are 0.47 and 0.4, respectively. The sharp-edged orifice elliptic jet of the present study will have very thin initial momentum thickness which will trigger the generation of very slender vortex rings and this will, in turn, result in high vorticity and higher Strouhal number for the sharp-edged orifice elliptic jet compared to the contoured nozzle elliptic jet of Hussain and Husain [8].

5. Phase-averaged quantities

The previous two sub-sections have pointed out the existence of coherent structures in the near flow field of the present elliptic jet. This section will describe the phase-averaging procedure for obtaining the quantities that characterize these coherent structures. The phased-averaged quantities will then be presented and discussed.

5.1. Phase-averaging procedure

Depending upon whether the hot-wire sensors were in the X–Y or X–Z plane, either the spanwise fluctuating (v') or lateral fluctuating (w') velocity signal was used to provide the phase on which the averaging procedure was based. Similar to the procedure used by Kiya and Matsumura [31], the incoming v' or w' signal was digitally band-pass filtered to obtain the filtered v'_f or w'_f signal, where the subscript f means filtered value. The digital band-pass filtering procedure involved obtaining the Fast Fourier Transform (FFT) of the v'or w' signal, then discarding unwanted frequencies using the Strouhal frequency ($f_\mathrm{o} = 648.4$ Hz) as the center frequency of the band-pass filter, which had a bandwidth of 200 Hz, and applying the inverse FFT to obtain v'_f or w'_f signal. After acquiring the filtered fluctuating velocity signal, its time derivative was obtained from the “smooth” function according to the formula:

$$\frac{\mathrm{d}y_t}{\mathrm{d}t} = \frac{2y_{t+2} + y_{t+1} - y_{t-1} - 2y_{t-2}}{10} \tag{5.1}$$

where y_t is v'_f or w'_f at time t. Two consecutive time instants, t_1 and t_2 ($> t_1$) were then determined such that the following two conditions were satisfied for the conditioning signal (note that the equations below are shown for only one of the signals, v'_f):

$$v'_\mathrm{f} = 0, \qquad \frac{\mathrm{d}v'_\mathrm{f}}{\mathrm{d}t} > 0, \tag{5.2}$$

$$v'_\mathrm{f} = 0, \qquad \frac{\mathrm{d}v'_\mathrm{f}}{\mathrm{d}t} < 0. \tag{5.3}$$

The time interval (t_2–t_1) had an average value of $\frac{1}{2}T_\mathrm{o}$, where $T_\mathrm{o} = 1/f_\mathrm{o}$. The phase ($\varphi$) was initially set to zero and then incremented by $\pi/phaseinc$, where *phaseinc* was selectable by software and was set equal to 200 in the present study, until $\varphi = 2\pi$. This made available 400 periods for phase-averaging. For each phase value, the corresponding time value was calculated in the following manner:

For $t_2 > t > t_1$, $\varphi < \pi$

$$t = \frac{\varphi(t_2 - t_1)}{\pi} + t_1. \tag{5.4}$$

For $t_1 > t > t_2$, $\varphi > \pi$

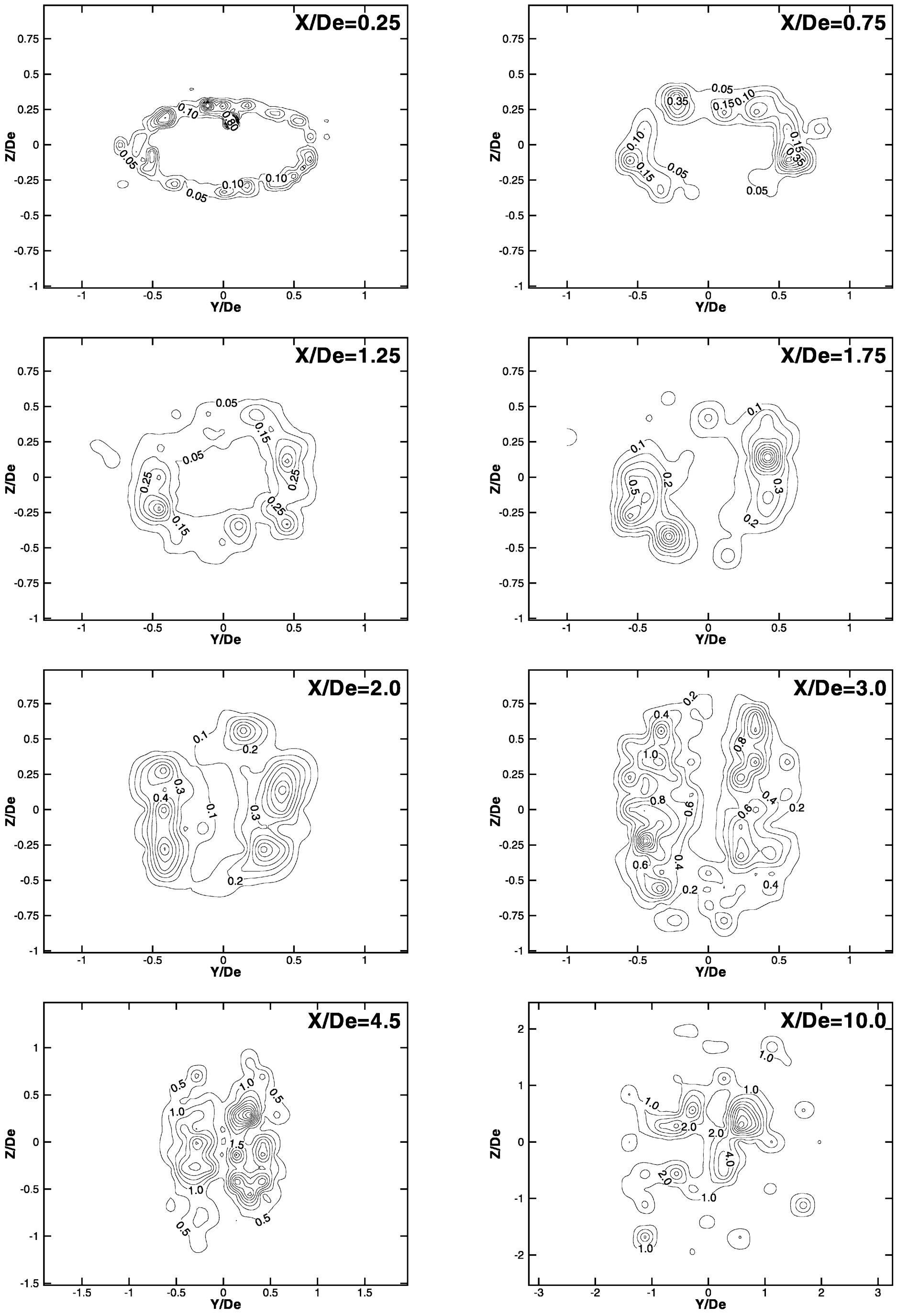

Fig. 23. Coherent streamwise normal stress ($(u_{\mathrm{c}}'^2/U_{\mathrm{cl}}^2) \times 1000$) contour maps.

$$t = \frac{(\varphi - \pi)(t_1 - t_2)}{\pi} + t_2. \tag{5.5}$$

It is clear from (5.4) and (5.5) above that t represents a value between t_2 and t_1 or between t_1 and t_2 such that the desired phase is obtained for averaging. Quantities of interest, such as u, v, w, uv and uw, were obtained from the digital hot-wire time series data by summing the results over all periods. The average values of these quantities were obtained by dividing the summed values by the number of available periods. Each hot-wire digital time series data set

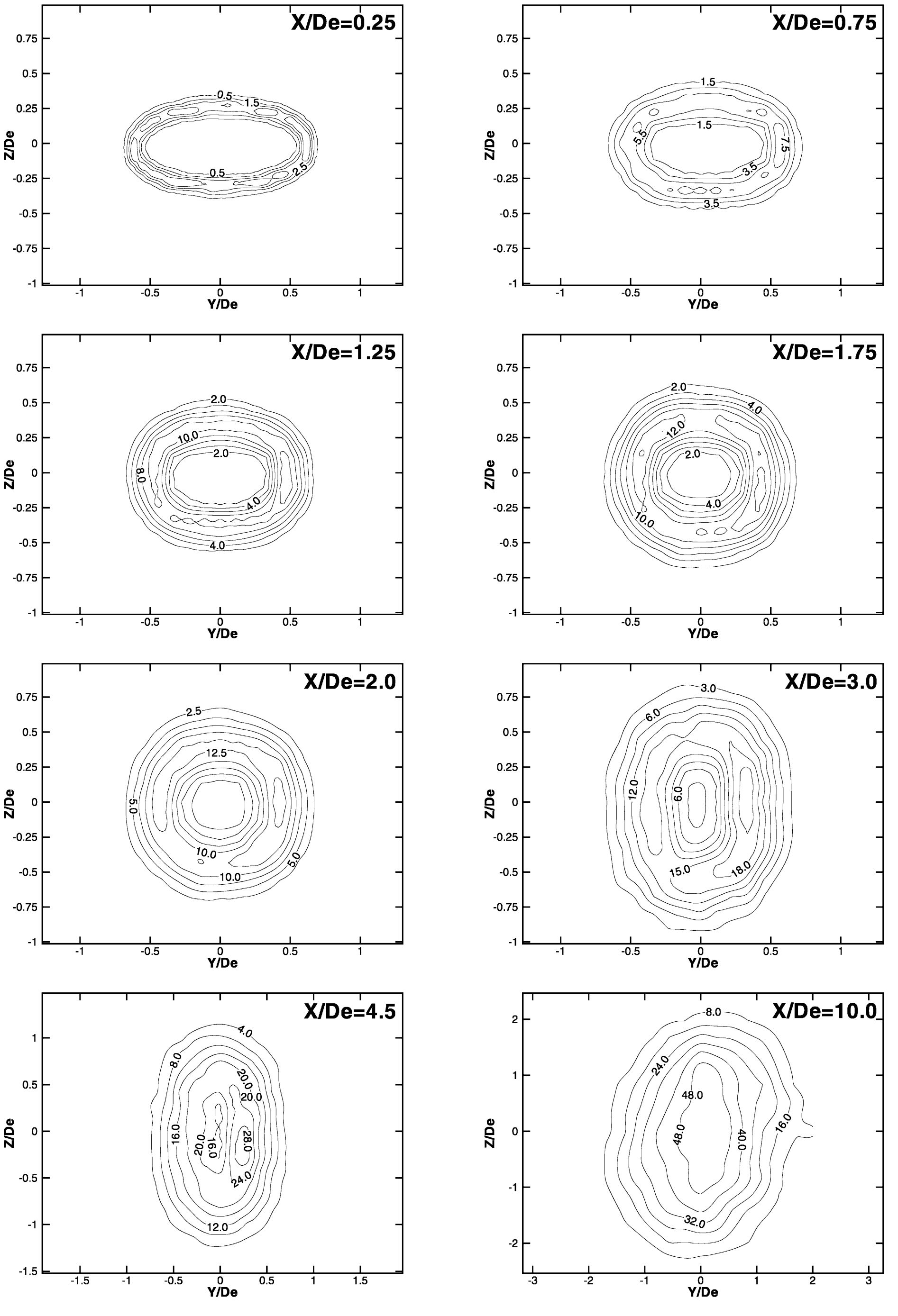

Fig. 24. Random streamwise normal stress $((u_r'^2/U_{cl}^2) \times 1000)$ contour maps.

consisted of 8192 samples (or 2.048 seconds of data). The triple decomposition technique for instantaneous signals, proposed by Reynolds and Hussain [32] was used to obtain the periodic and random components presented below.

As was done by Kiya and Matsumura [31], it was also assumed in the present study that although coherent structures lack perfect periodicity both spatially and temporally due to dispersions in their attributes, such as shape, size, orientation, etc., such dispersions will be small. A single X-wire probe, as opposed to a rake of hot-wire probes, was therefore used to obtain data for phase-averaging at various locations in the near field of the present flow.

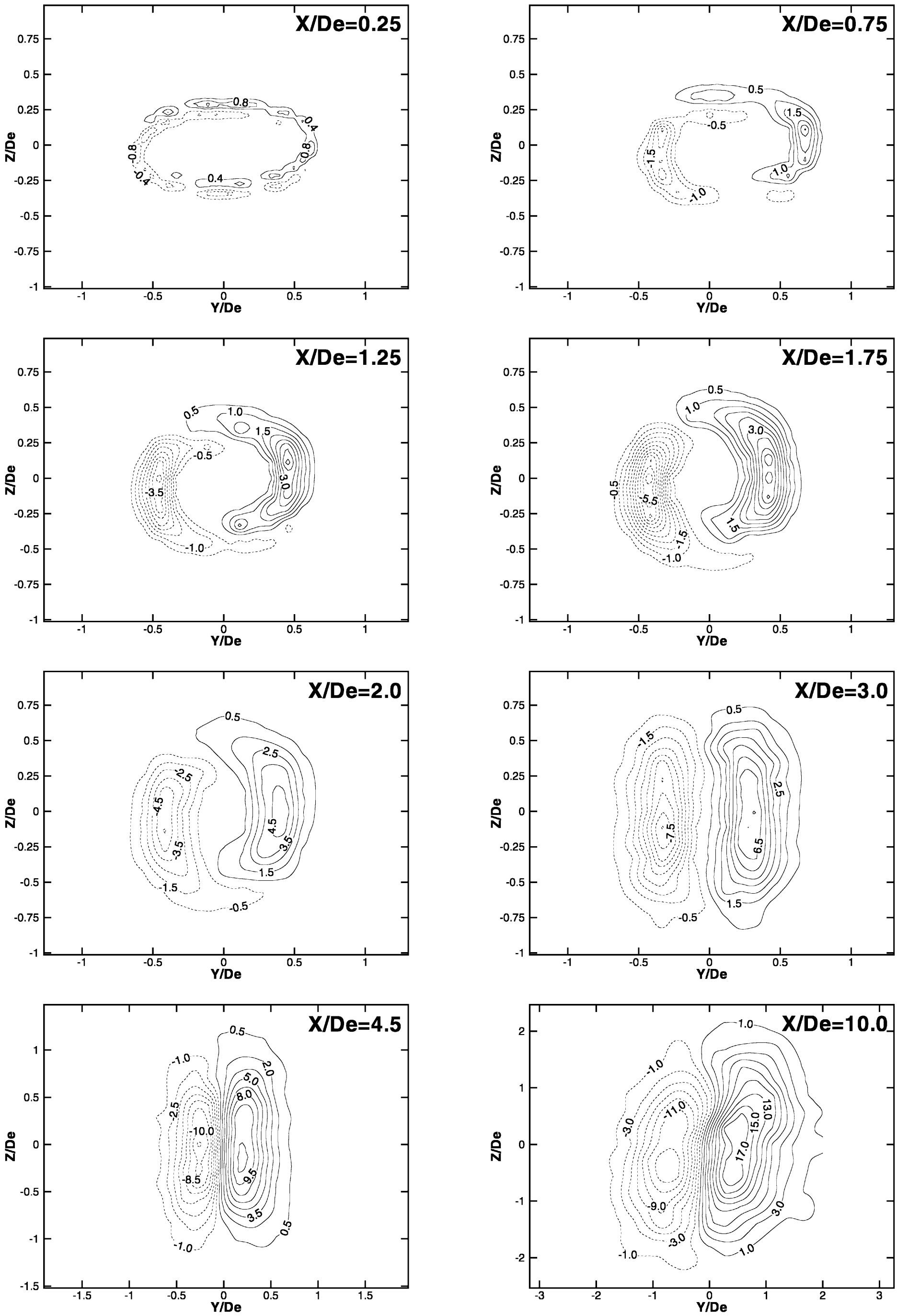

Fig. 25. Coherent spanwise primary shear stress ($(u'v'_c/U_{cl}^2) \times 1000$) contour maps.

5.2. Phase-averaged quantities results and discussion

Contour maps for the coherent ($u_c'^2$) and random ($u_r'^2$) contributions to the streamwise Reynolds normal stress, which was presented in Fig. 16 are shown in Figs. 23 and 24, respectively. The coherent and random streamwise normal stresses are normalized by U_{cl}^2 and amplified by a factor of 1000. The coherent and random contributions to the spanwise and lateral Reynolds normal stresses have also been measured but the results are not presented here for space reasons. The shapes of the contour maps of both the coherent and random streamwise normal stresses are

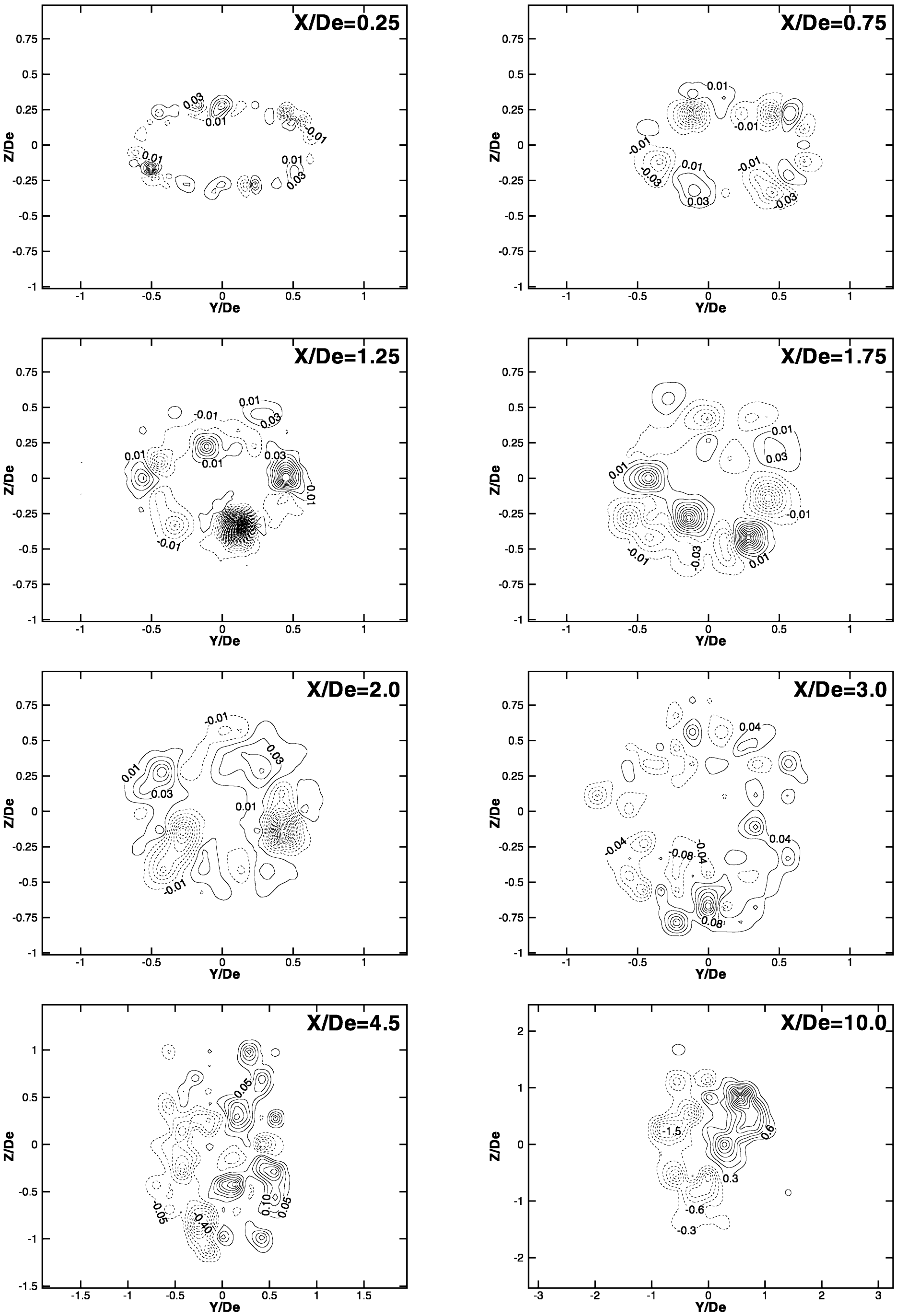

Fig. 26. Random spanwise primary shear stress ($(u'v'_r/U_{cl}^2) \times 1000$) contour maps.

similar to those of the streamwise Reynolds normal stresses at the corresponding locations. This suggests, as should be evident from applying the triple decomposition technique to the governing equations of motion, that the coherent and random streamwise normal stresses are produced in a manner similar to that of the streamwise Reynolds normal stress, namely, from the local shear in the mean streamwise velocity. The random streamwise normal stresses are much larger than their coherent counterparts at all the eight locations at which data were acquired, indicating that the random normal stresses make the dominant contribution to momentum transfer by the normal stresses in the near field of the present flow. This result is in agreement with that of Hussain and Zaman [33] for a circular jet and with that of Husain and Hussain [9] for an elliptic jet. It should be noted that the sum of the random and coherent streamwise normal stresses is approximately equal to the Reynolds normal stress at the corresponding locations in the flow, as is to be expected.

Contour maps for the coherent $(u'v'_c)$ and random $(u'v'_r)$ spanwise primary shear stress are shown in Figs. 25 and 26, respectively. The coherent and random spanwise primary shear stresses are normalized and amplified in the same way as the coherent and random streamwise normal stresses. While the shapes of the spanwise Reynolds primary shear stresses, shown in Fig. 17, and coherent spanwise primary shear stress contour maps (Fig. 25) are similar, suggesting that both of these quantities are produced by the same physical mechanism, the distribution of the random spanwise primary shear stress is "spotty". The coherent spanwise primary shear stress is very much larger than its random counterpart at all the eight locations shown in Figs. 25 and 26. This has also been observed in a circular jet by Hussain and Zaman [33] and in an elliptic jet by Husain and Hussain [9] and indicates that momentum transfer by the spanwise primary shear stress occurs mainly via the coherent spanwise primary shear stress in the near flow field of the present elliptic jet.

6. Conclusions

A detailed experimental study of a turbulent free jet of air issuing from a sharp-edged elliptic orifice plate into still air surroundings has been done. For comparison, some experiments were performed in round jets issuing from a sharp-edged orifice and from a contoured nozzle. An X-wire probe was used to acquire the three components of the mean velocity vector, time-averaged and phase-averaged quantities, autocorrelation coefficients and one-dimensional spectra of the fluctuating streamwise velocities. A pitot-static tube was used to obtain the mean static pressure data. To the extent that data have been acquired across entire planes at each streamwise location, not just along lines of symmetry as was done in many previous studies, the results presented here can be considered comprehensive for this noncircular jet.

The results show that mixing, as defined in the introduction section of this paper, in an elliptic jet issuing from a sharp-edged orifice plate is higher than in elliptic jets issuing from contoured elliptic nozzles and in round jets. The mean streamwise velocity decay rates along the jet centerline, the behavior of the turbulence intensities and the mean static pressure on the jet centerline, the potential core lengths and the spreading rates provide the evidence for this conclusion. The axisymmetric instability mode, which triggers the formation of symmetric shear layer structures, dominates the near field and transition regions of the present elliptic jet issuing from a sharp-edged orifice plate, at least up to $X/D_e = 4.5$. Furthermore, coherent structures are present in the near field of the elliptic jet and the random components of these coherent structures dominate the process of momentum transfer by the normal stresses while the coherent or periodic components are mainly responsible for momentum transfer by the shearing stresses.

Acknowledgements

The support of the Natural Sciences and Engineering Research Council of Canada (NSERC) through research grants awarded to the author is gratefully acknowledged. The author also wishes to thank all of the three anonymous referees whose suggestions and criticisms have led to a significant improvement of the quality of the original manuscript.

References

[1] W.R. Quinn, J. Militzer, Effects of nonparallel exit flow on round turbulent free jets, Int. J. Heat Fluid Flow 10 (2) (1989) 139–145.
[2] J. Mi, G.J. Nathan, D.S. Nobes, Mixing characteristics of axisymmetric free jets from a contoured nozzle, an orifice plate and a pipe, J. Fluids Engrg. 123 (2001) 878–883.
[3] W.R. Quinn, Upstream nozzle shaping effects on near field flow in round turbulent free jets, Eur. J. Mech. B Fluids (2006) 279–301.
[4] E.J. Gutmark, F.F. Grinstein, Flow control with noncircular jets, Annu. Rev. Fluid Mech. 31 (1999) 239–272.
[5] D.G. Crighton, Instability of an elliptic jet, J. Fluid Mech. 59 (1973) 665–672.
[6] P.J. Morris, Instability of elliptic jets, AIAA J. 26 (1988) 172–178.
[7] C.-M. Ho, E. Gutmark, Vortex induction and mass entrainment in a small-aspect-ratio elliptic jet, J. Fluid Mech. 179 (1987) 383–405.
[8] F. Hussain, H.S. Husain, Elliptic jets. Part 1. Characteristics of unexcited and excited jets, J. Fluid Mech. 208 (1989) 257–320.
[9] H.S. Husain, F. Hussain, Elliptic jets. Part 2. Dynamics of coherent structures: Pairing, J. Fluid Mech. 233 (1991) 439–482.

[10] H.S. Husain, F. Hussain, Elliptic jets. Part 3. Dynamics of preferred mode coherent structure, J. Fluid Mech. 248 (1993) 315–361.

[11] W.R. Quinn, On mixing in an elliptic turbulent free jet, Phys. Fluids A 1 (1989) 1716–1722.

[12] S.-J. Lee, S.-J. Baek, The effect of aspect ratio on the near-field turbulent structure of elliptic jets, Flow Meas. Instrum. 5 (1994) 170–180.

[13] J.-H. Yoon, S.-J. Lee, Investigation of the near-field structure of an elliptic jet using stereoscopic particle image velocimetry, Meas. Sci. Technol. 14 (2003) 2034–2046.

[14] P. Bradshaw, An Introduction to Turbulence and its Measurement, Pergamon Press, Oxford, 1975.

[15] P.W. Bearman, Corrections for the effect of ambient temperature drift on hot-wire measurements in incompressible flow, DISA Info. 11 (1971) 25–30.

[16] J.H. Bell, R.D. Mehta, Three-dimensional structure of plane mixing layers, JIAA Report TR-90, Dept. of Aeronautics and Astronautics, Stanford University, 1989.

[17] P.D. Clausen, D.H. Wood, The correction of X-probe results for transverse contamination, J. Fluids Engrg. 111 (1989) 226–229.

[18] U.R. Müller, On the accuracy of turbulence measurements with inclined hot wires, J. Fluid Mech. 119 (1982) 155–172.

[19] S.J. Kline, F.A. McClintock, Describing uncertainties in single-sample experiments, Mech. Engrg. 75 (1953) 3–8.

[20] J.F. Foss, D. Korschelt, Instabilities in the slit-jet flow field, J. Fluid Mech. 132 (1983) 79–86.

[21] S.C. Crow, F.H. Champagne, Orderly structure in jet turbulence, J. Fluid Mech. 48 (1971) 547–591.

[22] B.J. Hill, Measurement of local entrainment rate in the initial region of axisymmetric turbulent air jets, J. Fluid Mech. 51 (1971) 773–779.

[23] E. Gutmark, C.-M. Ho, Visualization of a forced elliptic jet, AIAA J. 24 (1986) 684–685.

[24] P. Bradshaw, D.G. Goodman, The effect of turbulence on static-pressure tubes, Aeronautical Research Council Reports and Memoranda, No. 3527, September, 1966.

[25] T. Christiansen, P. Bradshaw, Effect of turbulence on pressure probes, J. Phys. E: Sci. Instrum. 14 (1981) 992–997.

[26] P. Bradshaw, Turbulent secondary flows, Annu. Rev. Fluid Mech. 19 (1987) 53–74.

[27] H.J. Perkins, The formation of streamwise vorticity in turbulent flow, J. Fluid Mech. 44 (1970) 721–740.

[28] G. Raman, E.J. Rice, E. Reshotko, Mode spectra of natural disturbances in a circular jet and the effect of acoustic forcing, Exp. Fluids 17 (1994) 415–426.

[29] D. Liepmann, M. Gharib, The role of streamwise vorticity in the near-field entrainment of round jets, J. Fluid Mech. 245 (1992) 643–668.

[30] L.W.B. Browne, R.A. Antonia, L.P. Chua, Calibration of X-probes for turbulent flow measurements, Exp. Fluids 7 (1989) 201–208.

[31] M. Kiya, M. Matsumura, Incoherent turbulence structure in the near wake of a normal plate, J. Fluid Mech. 190 (1988) 343–356.

[32] W.C. Reynolds, A.K.M.K. Hussain, The mechanics of an organized wave in turbulent shear flow. Part 3. Theoretical models and comparisons with experiments, J. Fluid Mech. 54 (1972) 263–288.

[33] A.K.M.F. Hussain, K.B.M.Q. Zaman, Vortex pairing in a circular jet under controlled excitation. Part 2. Coherent structure dynamics, J. Fluid Mech. 101 (1980) 493–544.